International Journal of Heat and Mass Transfer 117 (2018) 799–817

Contents lists available at ScienceDirect

International Journal of Heat and Mass Transfer

journal homepage: www.elsevier.com/locate/ijhmt

Lattice Boltzmann simulations of flow and heat transfer from a permeable triangular cylinder under the influence of aiding buoyancy

T.R. Vijaybabu, K. Anirudh, S. Dhinakaran *

The Centre for Fluid Dynamics, Discipline of Mechanical Engineering, Indian Institute of Technology Indore, Simrol, Indore 453552, India

ARTICLE INFO

Article history:
Received 17 April 2017
Received in revised form 25 August 2017
Accepted 27 September 2017

Keywords:
Triangular cylinder
Apex facing flow
Side facing flow
Porous media
Mixed convection
Darcy-Forchheimer term
LBM

ABSTRACT

Mesoscopic numerical simulations have been carried out to learn about the flow and heat transfer characteristics of a 2-D permeable triangular cylinder, aligned at two different orientations under the influence of aiding buoyancy. Objective of this study is to investigate the effects of Darcy number and forebody shape on the hydrodynamic and thermal behaviour of the porous cylinder, under forced convection (*i.e.* $Ri = 0$) and aiding buoyancy conditions (Ri = 0.5 and 1) for a Prandtl number value of 0.71 (air). The ranges of Reynolds number (Re) and Darcy number (Da) considered in this study are $1 \leqslant Re \leqslant 40$ and $10^{-6} \leqslant Da \leqslant 10^{-2}$, respectively. Lattice Boltzmann method with two distribution functions is employed to perform the numerical experiments. Alongwith BGK collision operator, a body force term with viscous and inertial effects of the porous medium is employed at the porous zone. Detailed results are exhibited in the form of wake length, drag coefficient, streamlines, isotherm contours, heat transfer enhancement ratio and mean Nusselt number. Furthermore, a comparative investigation of drag coefficient and mean Nusselt number of permeable triangular cylinder (apex and side facing flow) with that of the square cylinder is carried out at $Da = 10^{-6}$ for different buoyancy levels. Under aiding buoyancy condition (*i.e.* $Ri > 0$), the side facing triangular cylinder experiences less drag force than the apex facing for all values of Da. A significant thermal dissipation is observed for increasing values of non-dimensional permeability (or Da) and Richardson number. Furthermore, simple expressions for mean Nusselt number, valid for the range of parameters embraced in the present study, are also provided. The appropriate selection of non-dimensional permeability under different buoyancy conditions is important while applying porous media modeling technique in diverse fields of engineering.

1. Introduction

Thermal incentives, motivated by material and energy saving deliberations, have led to efforts to look for different working fluids, utilisation of higher surface area and various configurations of elements in a system. The usage of working fluids, such as nanofluid and non-Newtonian fluid, have limitations in application inspite of their proven capability in improving heat transfer performance. The same or better augmentation in thermal behaviour of a system can be realised by choosing different fore-body and after-body shapes and orientations. For instance, considering the shape of body, convection heat dissipation of circular, diamond and triangular shaped bodies is more than that of the square-shaped [1]. Therefore, the intrinsic features, configuration of the body are considered to be important while modeling the problem in hand. Apart from modifying the shape of body, increasing its surface area aids improved fluid contact, resulting in effective transport of heat. As an illustration, pin fin arrangement is fitted on electronic chips in order to improve thermal characteristics. Such an arrangement of extended portions can be easily modeled by considering it as a porous body. Furthermore, it is evident from literature [2–4] that the configuration, porosity and permeability of porous body can be altered for the purpose of reaching higher heat performances. A working fluid with rich thermo-physical property shall additionally aid the thermal behaviour from this point. In conclusion, the knowledge of flow and heat transfer from porous bluff bodies with different cross-sections shall assist fellow scholars and engineers while using the porous media approach for seeking solution to real-time engineering problems.

Bao et al. [5] studied numerically the flow around an equilateral cylinder, at different angles (α) of flow, using a two-step Taylor-characteristic-based Galerkin method. It is seen that the triangular cylinder at $\alpha = 60^{\circ}$ (apex facing flow) experiences a lower drag force than the cylinder at $\alpha = 0^{\circ}$ (side facing flow). De and Dalal [6] analysed the flow pattern across a triangular cylinder with apex

* Corresponding author.
E-mail address: sdhina@iiti.ac.in (S. Dhinakaran).

https://doi.org/10.1016/j.ijheatmasstransfer.2017.09.115
0017-9310/

Nomenclature

Notations

AB & *AC*	front slant edges of apex facing cylinder
C_1 & C_2	binary constants
c_F	non-dimensional Forchheimer term
D	characteristic height of the cylinder, [m]
d_p	particle diameter, [m]
F_b	Boussinesq force term, [N]
$\tilde{f}_i$	particle density distribution function opposite to the direction i
F	body force due to the presence of the porous medium
F_r	resultant force acting on the cylinder, [N]
g	gravitational acceleration, [m s^{-2}]
g_i	temperature distribution function in direction i
G	body force due to gravity, [N]
K	permeability of the material, [m^2]
L_U	upstream length
N	number of lattices on the cylinder
p	dimensionless pressure, $\frac{p^*}{\rho v_\infty^2}$
PQ & *PR*	rear slant edges of side facing cylinder
Re	Reynolds number, $\frac{u_\infty D}{\nu}$
Ri	Richardson number, $\frac{g\beta\Delta\theta D}{v_0^2}$
u	non-dimensional x-component velocity, [m s^{-1}]
V	auxiliary velocity, [m s^{-1}]
x, y	horizontal & vertical coordinates
BC	rear flat edge of apex facing cylinder
C_D	coefficient of drag, $\frac{F_D}{0.5\rho v_0^2}$
c_s	speed of the sound [m s^{-1}]
Da	Darcy number, $\frac{K}{D^2}$
e_i	discrete lattice velocity in direction i, $\frac{\Delta x_i}{\Delta t}$
f_i	particle density distribution function in direction i
f_i^{eq}	equilibrium distribution function of density in direction i
F_i	total force term due to porous medium, [N]
F_y	drag force, [N]
g_i^{eq}	equilibrium distribution function of temperature in direction i
$\tilde{g}_i$	temperature distribution function opposite to the direction i
Gr	Grashof number, $\frac{g\beta\Delta\theta D^3}{\nu}$
L_D	downstream length
Ma	Mach number, $\frac{u}{c_s}$
Nu	local Nusselt number, $\frac{\partial\theta}{\partial n}$
Pr	Prandtl number, $\frac{\nu}{\alpha}$
QR	front flat edge of side facing cylinder
R_k	thermal conductivity ratio, $\frac{k_e}{k}$
T	dimensional temperature, [°C]
v	non-dimensional y-component velocity, [m s^{-1}]
w_i	weighing factor in direction i

Greek symbols

ρ	fluid density, [kg m^{-3}]
τ'	dimensionless relaxation time for temperature
Δt	time step, [s]
θ	dimensionless temperature, $\frac{T-T_\infty}{T_w-T_\infty}$
α	thermal diffusivity, [m^2 s^{-1}]
β	thermal expansion coefficient, [°C^{-1}]
Λ	viscosity ratio, $\frac{\mu_e}{\mu}$
τ	dimensionless relaxation time for density
Δx	lattice space
ν	fluid kinematic viscosity, [m^{2}s^{-1}]
ϕ	porosity
τ_t	non-dimensional time, $\frac{t v_\infty}{D}$
μ	fluid dynamic viscosity, [N s m^{-2}]

Subscripts

∞	far field value
M	mean value
w	wall
o	inlet value
i	lattice link direction
e	effective

Superscripts

$*$	dimensional form of variables

facing flow for *Re* = 10–250. They have reported that the critical Reynolds number at which flow shifts to unsteady regime is 38.9. Further, Tu et al. [7] analysed the flow characteristics and flow-induced forces of a stationary triangular cylinder with different incident angles (0–60°) at *Re* = 50–160. Their results show that the incident angle can greatly alter pressure distribution around the cylinder. For a example, the pressure stagnation point gradually moves from center of the windward surface (at $\alpha = 0^\circ$) to apex of the cylinder (at $\alpha = 60^\circ$) with increasing incident angles. Dhiman and Kumar [8] studied the effect of blockage ratio (cylinder to channel height ratio) on flow behaviour of non-Newtonian power-law fluids over a triangular cylinder for Reynolds number ranging between $1 \leqslant Re \leqslant 40$. They have found that the overall drag force decreases with the reduction in power-law index and/or blockage ratio. Also, it is evident from literature that the drag force experienced by triangular cylinder is lower than that of the square.

The triangular geometry is encountered in the novel heat exchangers (triangular pitch tube layout) and in pin-fin heat disposal used as sinks in electronic cooling [9] and porous heat sinks. Srikanth et al. [10] studied flow and heat transfer from a long equilateral triangle with apex facing flow for *Re* = 1–80 at a *Pr* value of 0.71 (air) for a blockage ratio of 0.25. Due to channel confinement, the critical value of *Re* is shifted to 58 from 38.9. This study also reveals that the triangular cylinder delivers heat transfer enhancement of 12.5% to 15% for $5 \leqslant Re \leqslant 45$ compared to square cylinder. Further, Zeitoun et al. [1] examined the heat transfer from a triangular cylinder with apex facing and side facing flow conditions for Reynolds number values up to 200 under uniform flow condition. They have formulated correlations for wake length, Strouhal number and Nusselt number for the ranges of parameters considered in their study. It has also shown that the apex facing flow has higher heat transfer rate than square and circular cylinder, and in the case of side facing flow, it is between square and circular cylinder. De and Dalal [11] have conducted a numerical study to see the effects of blockage ratio on flow and thermal dissipation traits from a solid triangular cylinder. Their results show that at a higher blockage ratio, vortex shedding suppresses for lower values of *Re*, due to viscous effects offered by the channel. However, the Strouhal number has shown increasing trend with blockage ratios for a constant *Re*. Also, they have reported that vortex shedding is the cause for change in Nusselt number on the rear face of triangular cylinder. Another unsteady flow and heat transfer case has been numerically investigated by Chatterjee and Mondal [12] for different values of Prandtl number (*Pr* = 0.71, 7 and 100). They have reported that the increase in *Re* affects the distribution of isotherms on the rear

surface and hence, the heat transfer is reducing. Besides, the Colburn j-factor which is used in process engineering design calculation has shown a linear decreasing trend with *Re*. Dhiman and Shyam [13] have also carried out a numerical investigation on heated triangular cylinder in order to deliver the effects of *Re* on thermal trends. The variations of surface Nusselt number at different periods of one cycle were also presented. It can be understood from above studies that the heat transfer performance is augmented for triangular cylinders and in unsteady regime, the overall thermal effect is not varying significantly with time. Prhashanna et al. [14] investigated the effects of power-law fluids over an equilateral triangle on flow separation, vortex shedding and heat transfer. They have concluded that the triangular cylinder with side facing flow delays the formation of wake with respect to the case of apex facing triangular cylinder. In addition, their analysis reveals that a 50–60% enhancement in heat transfer performance can be achieved by using non-Newtonian fluids. Thermal dissipation can also be increased by using Bingham plastic fluids [15] or by placing the cylinder near a stationary wall [16]. More recently, Bovand et al. [17] achieved heat transfer enhancement from apex, side and diagonal facing flow triangular cylinders by using Al_2O_3 nanofluid. Correlations for Nusselt number at different values of volume fractions and Reynolds number were also given by them. This study reveals that the nanoparticles significantly increase the heat transfer from a side facing triangular cylinder followed by the diagonal and apex facing triangular bodies. Gangawane [18] explored the mixed convective flow and heat transfer traits in top lid driven cavity containing heated triangular block subjected to constant heat flux boundary condition. Author has reported that by inserting a triangular cylinder with optimum blockage ratio of 10% can be suitable to control the convective flow and heat transfer in lid driven cavity. Cross buoyancy influence on flow and heat transfer characteristics of an equilateral triangle is presented by Chatterjee and Mondal [19] for *Re* values of 10 to 100 at $Pr = 0.71$. Their results show that the cylinder experiences negative lift forces due to the increment in Richardson number (*Ri*). Also, the Nusselt number value is more on the slanting faces of cylinder. However, heat transfer rate is more while increasing $Ri = 0$ to 1 for any fixed value of *Re*. From the above discussions, it can be understood that the thermal dissipation from a triangular cylinder is more due to the forebody and afterbody shapes. Additionally, rich thermal behaviour can be obtained by confining the channel, introducing buoyancy, using fluids with higher thermal conductivity and increasing the Prandtl number.

On parallel lines of the above discussion, a significant amount of research has also been undertaken with porous bluff bodies in order to receive better hydrodynamic and heat transfer characteristics. In the case of porous medium, flow and thermal behaviour is a function of *Re*, porosity (ϕ) and non-dimensional permeability (Darcy number – *Da*). It is evident from the literature [2,20–23] that more volume of fluid starts penetrating with less deviation into the cylinder while increasing *Da* value. Consequently, drag coefficient (C_D), lift coefficient (C_L), recirculation length (L_r) and intensity of vortex shedding are reduced. Also, a porous body with $Da = 10^{-6}$ exactly mimics a solid bluff body by restricting fluid flow through it. Moreover, due to its intrinsic flow regularization and heat transfer augmentation, porous medium can be found in various applications, viz., petroleum reservoir systems [24], design of nuclear biological chemical filters, gas-cooled reactor [21], cooling of electronic equipments [2]. Numerical analysis made by Dhinakaran and Ponmozhi [2] on heat transfer variation from an isolated permeable square cylinder reported that the percentage enhancement in heat transfer over impermeable cylinder at $Da = 10^{-4}, 10^{-3}$ and 10^{-2} is 3.31%, 19.91% and 108.4%, respectively. Apart from usual configurations like square and circle, researchers have also concentrated on various shapes like trapezoidal, sphere, diamond-shaped square porous bodies [4,25–29]. Very few studies can be seen on flow and heat transfer characteristics of porous body under buoyancy conditions [30–32]. Guerroudj and Kahalerras [30] have investigated the influence of porous block shape and its aspect ratio on a partially heated lower plate under different cross-flow buoyancy levels. Their results have shown that irrespective of the shape of porous body, the strength of vorticity is increasing with the increase in cross-buoyancy level and velocity of fluid. However, under different porous block properties such as aspect ratio, shape, permeability and thermal conductivity, the vorticity strength is found to be varying. They have revealed that the triangular shaped porous block aids for higher heat transfer rate than rectangular and trapezoidal blocks at lower values of permeability and *Re*. Further, Guerroudj and Kahalerras [31] analysed the effects of buoyancy and channel inclination on heat transfer behaviour from a heated porous block mounted on a channel. They have varied channel angle from -90° to $+90^\circ$ and Richardson number from 0 to 50. It is unveiled that for the porous blocks under aiding buoyancy conditions (*i.e.* at $+90^\circ$ channel angle), heat transfer rate is maximum and this can be further improved by increasing *Da* values. Their results again indicate rich thermal dissipation characteristics of triangular porous blocks than other shapes. From the above literature, it is clear that the heat transfer rate of permeable body is more than that of impermeable body. Importantly, the same performances can be tuned by varying permeability, buoyancy condition, configuration and placement of body. By considering these advantages, we propose to study the effects of buoyancy on flow and heat transfer characteristics of equilateral triangles with apex facing and side facing configurations. Triangular shape is chosen in the present numerical attempt due to its notable heat transfer enhancement over other regular shapes.

Flow through porous medium can be numerically modeled by supplementing Darcy-Forchheimer term to momentum equation [33–35]. The conventional numerical methods take large time to solve these equations due to their implicit nature. From a numerical perspective, complex flow geometries can be handled easily and effectively by using Lattice Boltzmann method (LBM). This method has been serving as a better alternative technique for solving transport equations since past three decades. Due to its inherent explicit nature [36], several researchers have been applying this approach to simulate porous media flow. For this purpose, Guo and Zhao [37] have coupled Darcy-Forchheimer term with collision equation of LBM. Later, Guo and Zhao [38] developed an LB model for convective heat transfer in porous media. To simulate heat transfer, one more distribution function is introduced which undergoes collision and streaming processes as like the distribution function for flow. It is to be noted that in case of stokes flow through porous medium, the introduction of effective viscosity parameter (μ_e) at free-fluid:porous medium interface is necessary in order to match the results of Brinkman equation with Stokes' equation to solutions of Darcy's law. Martys et al. [39] have reported that the Brinkman's equation is valid only when the value of μ_e is greater than the free-fluid viscosity. Spaid and Phelan [40] have modified the traditional LB equation to solve the Stokes/Brinkman formulation for flow in heterogeneous porous media. To reduce the magnitude of momentum at porous zone, they have modified the particle equilibrium distribution function. A similar kind of work can be found in [41], in which author has used pre-collision, post-collision and average velocities in the equilibrium distribution function for the purpose of obtaining appropriate resistance offered by the porous medium. Nie and Martys [42] analytically derived the exact macroscopic equations of the lattice Boltzmann model for the case of simple shear flows in porous media. They have found that the effective viscosity in the

governing equations is different from the one obtained from Chapman-Enskog relationship. It is noteworthy to mention that the literature [40–43] have concentrated on the shear flow or stokes flow through porous medium where the viscous effects are dominant, and thus, the evaluation of effective viscosity is crucial. However while keeping the viscosity ratio as unity, the LB model developed by Guo and Zhao [37] produces the results which are same as that of the solutions obtained from Navier-Stokes equations with Darcy-Forchheimer term. Fluid flow through thin porous media requires large number of grid points in order to model the same. Thus, to reduce computational cost, Yoshida and Hayashi [44] came up with permeable bounce-back scheme in which the porous material is treated through boundary condition rather than applying external force term. As per this boundary condition, a fraction of distribution function streams to the nearest nodes and the reminder of the distribution function are bounced back. Silva and Ginzburg [45] have analysed the bulk, boundary and interface properties of the Brinkman-based schemes in staircase discretization. They have evaluated the performances of numerical schemes based on accuracy of permeability predictions and the quality of velocity fields. More recently, Silva et al. [46] focused on the accuracy of reflection-type boundary conditions in the Stokes-Brinkman-Darcy modeling of porous flows solved with two-relaxation-time (TRT) LBM. Furthermore, there are few more approaches which are also developed from or coupled with the existing model in order to enhance numerical solutions [47–51]. Vortex shedding behind a porous square cylinder is probed by Babu and Narasimhan [52] at Re = 100 and 200. They have kept 32 number of lattices on front face of the cylinder in order to obtain results independent of grids as well as to avoid numerical instabilities. Accounting various advantages of LBM for porous medium flow, we have applied this method in the present numerical computations.

Objective of the present study is to investigate the effects of porous triangular cylinders with apex and side facing flow on flow pattern, drag coefficient, wake length, isotherm pattern, Nusselt number under different aiding buoyancy and non-dimensional permeability conditions. The LB model proposed by Guo and Zhao [37] is employed for this purpose.

2. Mathematical formulation

2.1. Problem description

Consider an equilateral triangle of side length 'D', maintained at a constant temperature of T_w, and exposed to a constant free stream v_∞ (fluid flow in positive y-direction) which is at an ambient temperature T_∞. The triangle is oriented at two different configurations – apex facing and side facing flow. The present study aims to simulate the flow and mixed convective heat transfer from the triangular cylinder placed in an unconfined domain. In order to make the problem computationally feasible, artificial boundaries are placed sufficiently far away from the cylinder. A pictorial representation of the computational setup alongwith various boundary conditions can be visualised in Fig. 1. The working fluid, air (Pr = 0.71), flows bottom to top and the gravitational force is meant to act opposite to the flow direction (aiding buoyancy condition). The following assumptions were made in order to make the problem amenable to numerical solutions:

(i) The problem under consideration is steady, laminar, two-dimensional, incompressible and the fluid is Newtonian. The fluid flows around and through an isotropic, homogenous porous matrix with constant porosity and permeability.

(ii) All the fluid properties are considered to be constant and the body forces are negligible, except for the body force terms in the collision equation (Boussinesq approximation in y-direction) in this study.

(iii) There is no heat generation in the porous cylinder and viscous dissipation in the porous zone is negligible. Further, the fluid phase temperature is equal to that of the porous phase (*i.e.* Local Thermal Equilibrium – LTE). This boundary condition should not be considered for rapid cooling or heating process or problems with significant temperature variation across the porous media [53]. However, the temperature difference between the fluid and porous phase in the present study is not significant and so the assumption is valid. The radiation from the permeable cylinder is negligible.

2.2. Conservation equations

Considering above assumptions, the following non-dimensional governing equations are used to represent flow and heat transfer phenomena [32]:

$$\frac{\partial u}{\partial x}+\frac{\partial v}{\partial y}=0, \tag{1}$$

$$\frac{\partial u}{\partial \tau_t}+\frac{1}{\phi}\left(u\frac{\partial u}{\partial x}+v\frac{\partial u}{\partial y}\right)=-\phi\frac{\partial p}{\partial x}+\frac{\Lambda}{Re}\left(\frac{\partial^2 u}{\partial x^2}+\frac{\partial^2 u}{\partial y^2}\right)-C_1\phi\frac{1}{ReDa}u - C_2\frac{1.75}{\sqrt{150}}\frac{1}{\sqrt{Da}}\times\frac{\sqrt{u^2+v^2}}{\sqrt{\phi}}u, \tag{2}$$

$$\frac{\partial v}{\partial \tau_t}+\frac{1}{\phi}\left(u\frac{\partial v}{\partial x}+v\frac{\partial v}{\partial y}\right)=-\phi\frac{\partial p}{\partial y}+\frac{\Lambda}{Re}\left(\frac{\partial^2 v}{\partial x^2}+\frac{\partial^2 v}{\partial y^2}\right)-C_1\phi\frac{1}{ReDa}v - C_2\frac{1.75}{\sqrt{150}}\frac{1}{\sqrt{Da}}\times\frac{\sqrt{u^2+v^2}}{\sqrt{\phi}}v+\phi Ri\theta, \tag{3}$$

$$\frac{\partial \theta}{\partial \tau_t}+\frac{1}{\phi}\left(u\frac{\partial \theta}{\partial x}+v\frac{\partial \theta}{\partial y}\right)=\frac{R_k}{Re\cdot Pr}\left(\frac{\partial^2 \theta}{\partial x^2}+\frac{\partial^2 \theta}{\partial y^2}\right). \tag{4}$$

For the introduction of porous resistance to the flow, Darcy-Brinkman- Forchheimer model has been used. The Darcy (coefficient of C_1) and Brinkman terms account for the viscous resistance, while the Forchheimer term (coefficient of C_2) looks after the inertial resistance to the flow. Here, C_1 and C_2 are the binary constants which hold the value of 0 at clear fluid zone and 1 at the porous zone. The dimensionless variables are defined as: $Re=\rho v_\infty D/\mu$ is the Reynolds number, $Pr=\mu C_p/k$ is the Prandtl number, $\Lambda=\mu_e/\mu$, denotes the viscosity ratio, $Ri=Gr/Re^2$ is the Richardson number. The viscosity ratio and thermal conductivity ratio are assumed to be unity in the present study. The above non-dimensional governing equations are obtained by introducing the following characteristic scales: $x=\frac{x^*}{D}, y=\frac{y^*}{D}, \tau_t=\frac{tv_\infty}{D}$, $p=\frac{p^*}{\rho v_\infty^2}, u=\frac{u^*}{v_\infty}, v=\frac{v^*}{v_\infty}, \theta=\frac{T-T_\infty}{T_w-T_\infty}$.

It is to be noted that the superscript $(*)$ indicates the dimensional form of the variable.

2.3. Boundary conditions

Inlet boundary: u = 0, v = 1 and $\theta=0$. Left and right boundaries: $\frac{\partial v}{\partial x}=0$, u = 0 and $\frac{\partial \theta}{\partial x}$. Outlet boundary: The gradient of velocity field is kept zero at exit of the domain $\left(i.e.\ \frac{\partial u}{\partial y}=\frac{\partial v}{\partial y}=\frac{\partial \theta}{\partial y}=0\right)$. For the temperature field, a constant temperature boundary condition is applied on the surface of the porous triangular cylinder. The cylinder exchanges heat with the cold fluid flowing through and around it, which is at a uniform temperature (T_∞) far away.

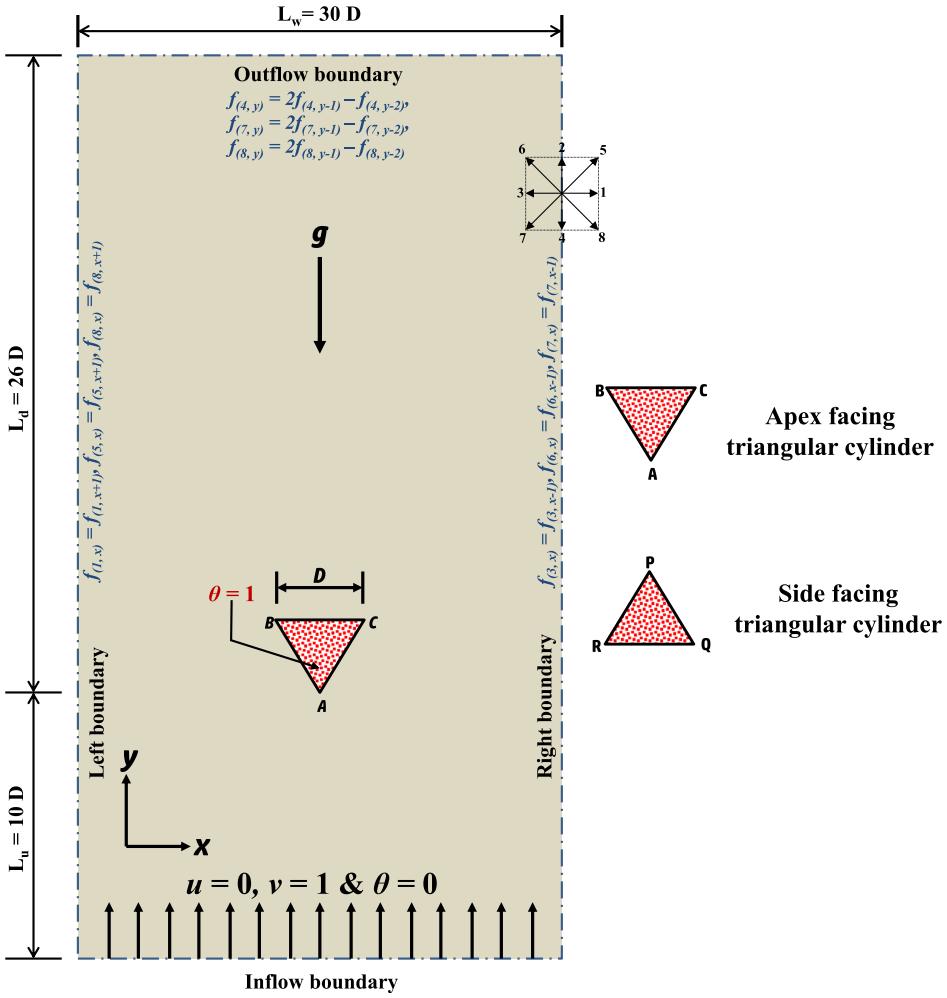

Fig. 1. Computational domain used in the analysis for mixed convection flow and heat transfer from a permeable triangular cylinder. Apex and side facing triangular permeable cylinder configurations are also shown in figure.

2.4. Lattice Boltzmann Method [LBM]

In our study, we have used a mesoscopic approach to characterize the flow and heat transfer behaviour. In LBM, a finite number of particles are considered as a single group and based on its distribution, the flow is modeled. For the temperature field, a separate distribution function is introduced, which receives the information of macroscopic properties of fluid such as density and velocity from the distribution functions of flow. LBM is advantageous over conventional numerical techniques while dealing with complex domains, flows through porous media and multi-phase flows.

2.4.1. LB flow evolution equation

In LBM, the grouped particles first undergo collision and then they stream to their neighbouring lattices based on the direction of particles. Extended flow evolution equation for the porous medium [37] can be expressed as

$$f_i(x + e_i\Delta t, t + \Delta t) - f_i(x,t) = -\frac{1}{\tau}\left[f_i(x,t) - f_i^{eq}(x,t)\right] + \Delta t F_i + \Delta t F_b. \tag{5}$$

In Eq. (5), f_i is the instantaneous particle distribution function of i^{th} link, f_i^{eq} is the corresponding equilibrium distribution and e_i are the velocity direction vectors of particles residing in a lattice. In the present study, we have used D2Q9 lattice model in which eight moving particles alongwith one rest particle exists and it can be seen in Fig. 1. Speed of the particles ($\Delta x_i/\Delta t$) can be written as

$$e_i = \begin{cases} (0,0), & i = 0 \\ (\cos[(i-1)\pi/2], \sin[(i-1)\pi/2])e, & i = 1-4 \\ (\cos[(2i-9)\pi/4], \sin[(2i-9)\pi/4])\sqrt{2e}, & i = 5-8. \end{cases} \tag{6}$$

The first term that appears to the right side of Eq. (5) is termed as BGK collision operator with Single Relaxation Time (SRT). In this model, a single relaxation factor τ is used to relax all particles towards equilibrium condition and this can be evaluated from the Chapman-Enskog relation, written as

$$\nu = \left(\tau - \frac{1}{2}\right)c_s^2\Delta t. \tag{7}$$

From above equation, the kinematic viscosity (ν) is evaluated based on a non-dimensional relaxation time (τ). Furthermore, c_s^2 is the speed of sound in lattice and it is equal to $e/\sqrt{3}$ in the case of D2Q9 model. However, to avoid stability issues of LBM, the schemes such as two-relaxation-time (TRT) and multi-relaxation-time (MRT) can be used. Also, as per literature [42,43] any of these models should be considered while dealing with viscous dominating porous flow or instances where the effective viscosity variation with permeability is taken into the account. In the present study we have considered the viscosity ratio as unity and also due to the ease of implementation of SRT model, we have used the same in present study. A force term F_i which accounts the drag effects due to

presence of porous medium is directly coupled with the BGK collision operator to recover fluid flow through the porous region. The force term that accounts for porosity (ϕ) of the porous medium can be expressed as

$$F_i = w_i\rho\left(1-\frac{1}{2\tau}\right)\left[3(e_i\cdot F)+\frac{9}{\phi}(e_i\cdot U)(e_i\cdot F)-\frac{3}{\phi}(U\cdot F)\right]. \quad (8)$$

Here, F is the body force due to the presence of porous medium which is otherwise termed as Darcy-Forchheimer force term. This can be written as

$$F = -\frac{\phi\nu}{K}U-\frac{\phi c_F}{\sqrt{K}}|U|U+\phi G, \quad (9)$$

where K is permeability of the porous medium, $c_F = 1.75/(\sqrt{150\times\phi^3})$ is the non-dimensional Forchheimer term defined by Fu et al. [54], $|U| = \sqrt{u^2+v^2}$ in which u and v are the components of U in x and y-directions, and G is the body force due to gravity. The equilibrium distribution function which appears on the right side of Eq. (5) should consider porosity of the porous medium. It can be written as follows:

$$f_i^{eq} = w_i\rho\left[1+3(e_i\cdot U)+\frac{9}{2\phi}(e_i.U)^2-\frac{3}{2\phi}(U\cdot U)\right]. \quad (10)$$

In the above equation, w_i is the weighting factor of each particle that resides in a lattice. In the case of D2Q9, $w_0 = 4/9$, $w_i = 1/9$ for i = 1–4 and $w_i = 1/36$ for i = 5–8. Once after performing the collision process, streaming operation takes place followed by the usage of appropriate boundary condition. Until this point of the code, we have retained fluid information in terms of distribution functions only. This calls the need for conversion of these mesoscopic terms into macroscopic properties. For instance, addition of distribution function values at a particular lattice provides the density (ρ) at that point. Therefore, the macroscopic properties are evaluated from the following equations:

$$\rho = \sum_{i=0}^{8} f_i. \quad (11)$$

where 'V' is the auxiliary velocity and it is defined as

$$\rho V = \sum_{i=1}^{8} e_i f_i + \frac{\Delta t}{2}\rho F. \quad (12)$$

The actual velocity components of porous medium can be calculated from the following equation:

$$U = \frac{V}{c_0+\sqrt{c_0^2+c_1|V|}}. \quad (13)$$

The two parameters c_0 and c_1 in Eq. (12) are given by

$$c_0 = \frac{1}{2}\left(1+\phi\frac{\Delta t}{2}\frac{\nu}{K}\right); \quad c_1 = \phi\frac{\Delta t}{2}\frac{c_F}{\sqrt{K}}. \quad (14)$$

In the case of natural convection, an extra force term (Boussinesq term) F_b is added to the collision equation, because, the flow is driven by temperature gradient. The same can be written as follows:

$$F_b = 3w_i g\beta\theta e_{iy}. \quad (15)$$

Here, e_{iy} is the velocity vectors acting in the y-direction.

2.4.2. LB equation for temperature field

To evaluate the temperature characteristics, another distribution function called $g(x,t)$ is introduced. In both forced and mixed convection, the energy equation can be solved once after the flow field is calculated. Density and velocity values obtained from the flow field distribution functions $f(x,t)$ are then used in the temperature distribution functions $g(x,t)$. The LB equation that describes the temperature field can be written as

$$g_i(x+e_i\Delta t, t+\Delta t) - g_i(x,t) = -\frac{1}{\tau'}\left(g_i(x,t)-g_i^{eq}(x,t)\right). \quad (16)$$

where τ' is the dimensionless relaxation time for temperature field and it is evaluated from thermal diffusion coefficient ($\alpha = (\tau-1/2)c_s^2\Delta t$). The temperature equilibrium distribution function g_i^{eq} in the Eq. (16) can be written as

$$g_i^{eq} = w_i\theta[1+3(e_i\cdot U)]. \quad (17)$$

where w_i is the same weighing factor which has been defined in the flow equilibrium distribution function and θ is the temperature of the fluid (non-dimensional), which can be calculated from the distribution function $g(x,t)$, can be written as

$$\theta = \sum_{i=0}^{8} g_i. \quad (18)$$

2.4.3. LBM boundary conditions

In conventional numerical techniques, the boundary conditions are specified in terms of macroscopic variables like density and velocity. But in the case of LBM, collision and streaming operation carries only the information of particle distributions. Hence, the boundary conditions are also needed to be specified in terms of distribution functions only. Various boundary conditions used in this study are described below.

2.4.4. Inlet boundary condition

The flow simulations carried out by LBM is weakly compressible in nature and therefore, the inlet velocity has to be chosen such that the Mach number (Ma), remains less than 0.1 [36]. A free uniform velocity (v_∞ or v_0) which has fewer compressibility effects is given to the inlet. At inlet, the distribution functions f_2,f_5 and f_6 falls inside the domain. As per Zou and He boundary condition [55], the initial values of density is calculated for further evaluation of unknown distribution functions. The inlet boundary condition can be written as follows:

$$\rho_0 = \frac{1}{1-v_0}[f_0+f_1+f_3+2(f_4+f_7+f_8)]; \quad (19)$$

$$f_2 = f_4+\frac{2}{3}\rho_0 v_0; \quad f_5 = f_7+\frac{1}{6}\rho_0 v_0; \quad f_6 = f_8+\frac{1}{6}\rho_0 v_0. \quad (20)$$

In the above equations, ρ_0 and v_0 are the initial density and velocity (in y-direction), respectively. Also, the temperature at inlet is fixed to zero (*i.e.* $\theta = 0$). The unknown distribution functions of temperature are specified as $g_2 = -g_4$, $g_5 = -g_7$ and $g_6 = -g_8$.

2.4.5. Left and right boundary

Artificial boundaries are placed sufficiently far away from the triangular cylinder, on the left and right side of the domain. Accordingly, slip boundary condition is employed where the velocity gradients normal to the flow direction are zero. In case of left boundary, the unknown distribution functions are f_1,f_5 and f_8. Hence, the gradient can be turned to zero by specifying, $f_{1,x} = f_{1,x+1}$, $f_{5,x} = f_{5,x+1}$ and $f_{8,x} = f_{8,x+1}$. Consequently, at right boundary, it is specified as $f_{3,x} = f_{3,x-1}$,$f_{6,x} = f_{6,x-1}$ and $f_{7,x} = f_{7,x-1}$. Furthermore, the adiabatic boundary condition (*i.e.* $\partial\theta/\partial x = 0$) is imposed on left and right boundaries of the computational domain. Corresponding boundary condition for left boundary can be written as, $g_{(1,x)} = g_{(1,x+1)}$, $g_{(5,x)} = g_{(5,x+1)}$ and $g_{(8,x)} = g_{(8,x+1)}$.

2.4.6. Outlet boundary condition

The distribution function that falls inside the domain at outlet boundary can be evaluated through extrapolation [36]. At the outlet of the domain, the unknown distributions are f_4, f_7 and f_8 which can be evaluated by using second order polynomial, and the same can be seen in Fig. 1. The thermal boundary condition at outlet is also specified in similar fashion. The unknown distribution functions of temperature at outlet can be written as, $g_{(4,y)} = 2g_{(4,y-1)} - g_{(4,y-2)}$, $g_{(7,y)} = 2g_{(7,y-1)} - g_{(7,y-2)}$ and $g_{(8,y)} = 2g_{(8,y-1)} - g_{(8,y-2)}$.

2.4.7. Boundary conditions at porous zone

The force term F_i, which appears in Eq. (5) is enabled at those lattices which falls inside the triangular porous zone. It is to be noted that the number of grids should be sufficiently large enough to avoid the staircase effects offered by the slant edges of triangular porous body. In the present code, the activation of F_i term is governed by an array called $w(i,j)$. Initially, this array is mentioned as zero in the entire computational domain. Meanwhile, the same array is switched to an integer value of 1 at those grid points which falls inside the porous zone. Furthermore, the non-dimensional temperature value of 1 (*i.e.* $\theta = 1$) is kept in the porous region. Hence, the temperature distribution functions in the porous zone is specified as

$$g_i + \tilde{g}_i = \text{Wall temperature} \times (w_i + \tilde{w}_i). \tag{21}$$

In the above equation, $\tilde{g}_i$ and $\tilde{w}_i$ denotes the opposite distribution function and weighing factor of lattice link of i, respectively. If the wall temperature is maintained as zero, this boundary condition turns to be, $g_i = -\tilde{g}_i$.

2.5. Dimensionless parameters

Some of the dimensionless parameters used in this study are defined as follows:

2.5.1. Reynolds number

Reynolds number (Re) can be written as

$$Re = \frac{v_\infty D}{\nu} = \frac{v_\infty N}{\nu}. \tag{22}$$

2.5.2. Darcy number

Darcy number (Da) is the non-dimensional permeability value and it can be expressed as

$$Da = \frac{K}{D^2} = \frac{K}{N^2}. \tag{23}$$

It can be seen from Eqs. (22) and (23) that the characteristic height of porous body D is replaced by N. In BGK-LBM, the numerical stability and accuracy of the results are mainly dependent on the number of lattices on characteristic length; in the present analysis, N represents the number of lattices that are present on characteristic length of the cylinder. The porosity (ϕ) and Darcy number of a porous medium made of packed bed of spherical particles can be related through Carman-Kozeny relation [56] given by

$$Da = \frac{1}{180}\frac{\phi^3 d_p^2}{D^2(1-\phi)^2}. \tag{24}$$

In the present study, we have considered the particle diameter size (d_p) as 1 cm (for $D = 1m$) [57] and with this relationship the porosity value is evaluated for a given value of Darcy number.

2.5.3. Drag coefficient

The momentum exchange between two opposing directions of neighbouring lattices aids for the evaluation of drag forces. In the current study, the momentum exchange method is employed for the calculation of total resultant force F_r, and it can be written as [58]

$$F_r = \sum_{\text{all } x_b}\sum_{i=1}^{8} e_i\left[\tilde{f}_i(x_b,t) + \tilde{f}_i(x_b + e_i\Delta t, t)\right] \times [1 - w(x_b + e_i)]\Delta x/\Delta t. \tag{25}$$

where $w(x_b + e_i)$ is an indicator, which is 0 at fluid nodes and 1 at porous nodes. Also, x_b indicates the porous boundary nodes and $\tilde{f}_i(x_b,t)$ is the post-collision distribution function. For a given non-zero velocity e_i, e_i denotes the lattice velocity in the opposite direction. From the total force, the drag coefficient is evaluated as

$$\text{Drag coefficient}, C_D = \frac{F_y}{0.5 \times \rho v_\infty^2 D}. \tag{26}$$

Here, F_y is the force acting in the y-direction.

2.5.4. Nusselt number

Heat transfer from the permeable cylinder to the flowing fluid can be evaluated through local Nusselt number given by $Nu = -R_k \frac{\partial\theta}{\partial n}$ [2]. Here, n is the direction normal to the cylinder surface and R_k is the ratio of thermal conductivity of the porous material (k_e) and fluid (k_f), which is assumed to be unity in this study. Average heat transfer at any face of the permeable body is obtained by taking average of the local Nusselt number along that face. The mean Nusselt number value (Nu_M), which represents the total heat transfer from the permeable cylinder is evaluated by taking average of surface Nusselt number of all edges.

2.5.5. Heat transfer enhancement ratio

In this study, the heat transfer enhancement obtained by a cylinder under buoyancy with reference to the cylinder without buoyancy (*i.e.* at $Ri = 0$) is expressed in terms of heat transfer enhancement ratio (E). It is given by the ratio of the Nusselt number of a cylinder in general (when $Ri > 0$) to Nusselt number of the cylinder at $Ri = 0$.

$$E = \frac{Nu}{(Nu)_{\text{at } Ri=0}}. \tag{27}$$

The present investigation elaborates on the variation of E at different faces of the cylinder and, hence, heat transfer enhancement ratio at different faces is represented as E_{AB}, E_{BC}, E_{CA} and E_{PQ}, E_{QR}, E_{RP} for apex and side facing flows, respectively.

3. Numerical procedure and validation

3.1. Numerical method

To conduct present numerical simulations, a FORTRAN code has been written based on Lattice Boltzmann method. Eq. (5) is applied to the entire computational domain for the collision operation. However, the porous force term that appears in the collision equation should not be applied in clear fluid region. For this purpose, a constant value of 0 is multiplied with porous force term F_i except the porous triangular region. Additionally, the buoyancy force term (F_b) is applied in the entire domain. In this study, BGK collision operator with single relaxation time (τ) has been used. The initial velocity (v_0) and kinematic viscosity (ν) are formulated based on the number of lattices on characteristic length (N). The Chapman-Enskog relationship [59] is used to calculate the non-dimensional relation factors (τ & τ'). Initially, the velocity values

(u and v) at all nodes are kept to be zero and the density value ρ is fixed 1. The $g\beta$ term that presents in Boussinesq force term in Eq. (5) can be evaluated through Richardson number. To avoid numerical instability issues, $\sqrt{g\beta\Delta TD}$ term should be less than 0.1 [36]. This is because, in an incompressible regime, this term is directly proportional to velocity. It is seen that the Lattice Boltzmann algorithm is relatively simpler than the conventional CFD methods. In this study, simulations are conducted until the following convergence is satisfied.

$$\frac{\sqrt{\sum_{i,j}\left[U_{i,j}^{k}-U_{i,j}^{k-100}\right]^{2}}}{\sqrt{\sum_{i,j}\left[U_{i,j}^{k}\right]^{2}}}\leqslant 1\times 10^{-6},\quad \frac{\sqrt{\sum_{i,j}\left[\theta_{i,j}^{k}-\theta_{i,j}^{k-100}\right]^{2}}}{\sqrt{\sum_{i,j}\left[\theta_{i,j}^{k}\right]^{2}}}\leqslant 1\times 10^{-6}. \tag{28}$$

Here, $U_{i,j}$ is the fluid velocity; $\theta_{i,j}$ is the fluid temperature and k is the iteration level.

3.2. Grid sensitivity analysis

A grid independent study is carried out at Re = 30, $Da = 10^{-6}$ and Ri = 1 to check the flow and heat transfer parameters such as C_D and Nu_M on the number of lattice and downstream length (L_D). In this study, we have performed systematic test simulations by varying number of lattices (N) placed on the characteristic length of the cylinder (both apex facing and side facing triangular cylinder cases) from 30 to 70 for L_D values of 15, 25 and 35. Tables 1 and 2 suggest that 40 lattices with downstream length of 25D will produce results independent of lattice units variation with less computational efforts. In LBM, based on number of lattices (N), the non-dimensional relaxation time (τ) varies and so does the stability and accuracy of the solution. For instance, if we choose more lattices, the kinematic viscosity value reduces for a constant value of Re with an initial velocity less than 0.1. Accordingly, it will take more time to reach the convergence limit due to reduction in τ. Due to this large computational time, the variation in distribution functions produces stability issues. To avoid such occurrences we have chosen non-dimensional relaxation values for flow and temperature, which are 0.56 and 0.5845, respectively.

3.3. Validation of numerical results

In order to verify validity of the present LBM code, the obtained numerical results are compared with literature. In this section, we have validated our code by comparing C_D and Nu_M values of porous square cylinder under different Da and Ri values. Also, we have verified the present results of triangular cylinder (both apex and side facing flow configurations) under forced convection condition with published results. Tables 3 and 4 show the percentage deviation of drag coefficient and Mean Nusselt number values from the literature at $Da = 10^{-3}$ & 10^{-2} and Ri = 0 & 1. It is clear from Tables 3 and 4 that the numerical results of current study are in good agreement with Dhinakaran and Ponmozhi [2] and Sharma et al. [60]. Furthermore, Fig. 2(a) and (b) compares C_D and Nu_M results of impermeable triangular cylinder at different values of Re for Pr = 0.71. This graphical illustration clearly indicates that the present results are showing very less deviation from results obtained by Zeitoun et al. [1,11] and De and Dalal [17]. A maximum error of 2.995% and 3.4% is obtained in the case of drag coefficient and mean Nusselt number respectively, and this deviation is due to the numerical approach and discretization schemes. It is worth to mention that the literature considered for numerical result comparison have used finite volume approach; whereas, the present results are obtained from LBM simulations. We have validated the present LB code for Couette flow (cavity filled with porous medium) with analytical solutions. Fig. 3(a) shows the velocity profiles of the Couette flow at Re = 10 for different values of Da. Symbols represent the results from the present code and the lines indicate analytical solution. The equation for analytical solution has been taken from the Eq. (24) of LB model proposed by Guo and Zhao [37]. Further, velocity at the midway of the centre against Darcy number at Re = 0.1 is compared with the results obtained by Guo and Zhao [37] (see in Fig. 3(b)). We have found excellent agreement between present results with the analytical solutions as well as results at low Reynolds number.

4. Numerical results and discussions

The 2-D numerical simulations are carried out for flow across the two permeable triangular cylinder configurations [(i) apex facing flow and (ii) side facing flow] in an unconfined vertical flow regime, under the influence of aiding buoyancy for the following range of physical parameters:

- Reynolds number, Re = 1–40.
- Richardson number, Ri = 0, 0.5 and 1.
- Darcy number, $Da = 10^{-6}, 10^{-4}, 10^{-3}$ and 10^{-2}.
- Porosity, $\phi = 0.629$, 0.935, 0.977 and 0.993. (these values are evaluated from Carman-Kozeny relation)
- Prandtl number, Pr = 0.71 (air).

We have selected the Reynolds number up to 40, in order to see the variations of flow characteristics in steady flow regime. From literature [2,20–23], it is evident that the range of Da values that we have selected covers all the permeability conditions *i.e.*, solid-like to highly permeable. The non-dimensional parameters viz., Re and Da have been selected on the basis of applications related

Table 1
Lattice dependence analysis for apex facing triangular configuration.

S. No.	N	L_D	C_D	% variation	Nu_M	% variation
1	35	15	3.795	1.119	3.326	1.627
2	40	15	3.758	0.133	3.374	0.207
3	45	15	3.751	0.053	3.380	0.03
4	70	15	3.753	–	3.381	–
5	35	25	3.764	0.615	3.382	0.763
6	40[a]	25	3.742	0.027	3.406	0.059
7	45	25	3.741	0	3.409	0.029
8	70	25	3.741	–	3.408	–
9	35	35	3.760	0.615	3.386	0.75
10	40	35	3.740	0.08	3.410	0.047
11	45	35	3.739	0.054	3.411	0.018
12	70	35	3.737	–	3.412	–

[a] Number of lattices placed on characteristic length of the cylinder in this study.

Table 2
Lattice independence analysis for side facing triangular configuration.

S. No.	N	L_D	C_D	% variation	Nu_M	% variation
1	35	15	3.467	1.404	3.097	2.179
2	40	15	3.416	0.088	3.142	0.758
3	45	15	3.420	0.029	3.162	0.126
4	70	15	3.419	–	3.166	–
5	35	25	3.436	0.999	3.130	2.065
6	40[a]	25	3.405	0.088	3.193	0.094
7	45	25	3.400	0.059	3.195	0.031
8	70	25	3.402	–	3.196	–
9	35	35	3.429	0.823	3.138	1.999
10	40	35	3.402	0.029	3.202	0
11	45	35	3.401	0	3.200	0.062
12	70	35	3.401	–	3.202	–

[a] Number of lattices placed on characteristic length of the cylinder in this study.

Table 3
Comparison of calculated drag coefficient (C_D) values of permeable square cylinder with literature at different values of Da and Ri values.

Re	C_D					
	Ri = 0 and $Da = 10^{-2}$			Ri = 1, impermeable cylinder		
	a^a	b^b	% deviation	a^a	c^c	% deviation
5	4.055	4.074	0.476	10.406	10.426	0.19
10	2.796	2.82	0.855	6.875	6.943	0.999
20	2.049	2.065	0.799	4.875	4.928	1.089
30	1.725	1.741	0.884	3.995	4.093	2.433
40	1.472	1.486	0.938	3.534	3.6	1.862

Table 4
Comparison of calculated mean Nusselt number (Nu_M) values of permeable square cylinder with literature at different values of Da and Ri values.

Re	Nu_M					
	Ri = 0 and $Da = 10^{-3}$			Ri = 1, impermeable cylinder		
	a^a	b^b	% Deviation	a^a	c^c	% deviation
5	1.223	1.196	2.213	1.422	1.418	0.295
10	1.654	1.617	2.238	1.867	1.851	0.87
20	2.325	2.301	1.019	2.479	2.463	0.663
30	2.866	2.816	1.728	2.939	2.91	0.983
40	3.242	3.199	1.328	3.306	3.284	0.67

a^a Present study.
b^b Dhinakaran and Ponmozhi [2].
c^c Sharma et al. [60].

to electronic cooling, particularly related to heat sinks (e.g. porous and pin-fin heat sinks). Aiding buoyancy has pronounced effects while shifting from forced convection condition, further increment in buoyancy does not cause much significance on flow and thermal characteristics [60]. By considering all these factors, we have chosen the above mentioned parameter ranges. This numerical study will serve us to gauge the effects of buoyancy and permeability on flow and thermal patterns. The results are labelled into flow and heat transfer characteristics and are presented as follows:

4.1. Flow characteristics

In this section, a detailed discussion on the influence of Reynolds number (Re), Darcy number (Da), Richardson number (Ri) and configuration of triangular porous body on flow behaviour is presented in both qualitative and quantitative manner.

4.1.1. Streamline pattern

Fig. 4 presents the representative flow patterns in the vicinity of permeable triangular cylinder with apex facing and side facing flow, through streamline contours for different values of Richardson number (Ri = 0, 0.5 and 1) and Darcy number ($Da = 10^{-6}, 10^{-4}, 10^{-3}$ and 10^{-2}) at Re = 40. In the case of apex facing triangular cylinder, fluid approaches the slanting faces of the cylinder and hence, it moves smoothly. It should be noted that due to these slant edges, the viscous boundary layer becomes thin. However, fluid starts separating at the end of slanting faces of the cylinder. Turning to the side facing flow case, fluid patterns separate at the edge of cylinder immediately after approaching the flat face. In both configurations, two standing and symmetric vortices form at the downstream of cylinder while increasing fluid momentum. This is the scenario of flow over triangular bluff bodies and the same qualitative results have been addressed in several studies [5–8,11]. The above flow phenomena are exactly similar to the traits displayed by flow across the porous cylinder at $Da = 10^{-6}$. It is clear that at such low levels of permeability, the porous cylinder mimics its solid counterpart and the same has been reported by several researchers for other porous bluff body shapes [20–23,25–29]. As permeability of the porous zone is increased, fluid starts entering into the cylinder. For example, at $Da = 10^{-4}$ and Re = 40, fluid penetration through the cylinder is evident. However, due to presence of the viscous force in porous body, fluid deviation is found to be more. A further rise in Da, suppresses this viscous force and consequently, the deviation of fluid is observed to be less.

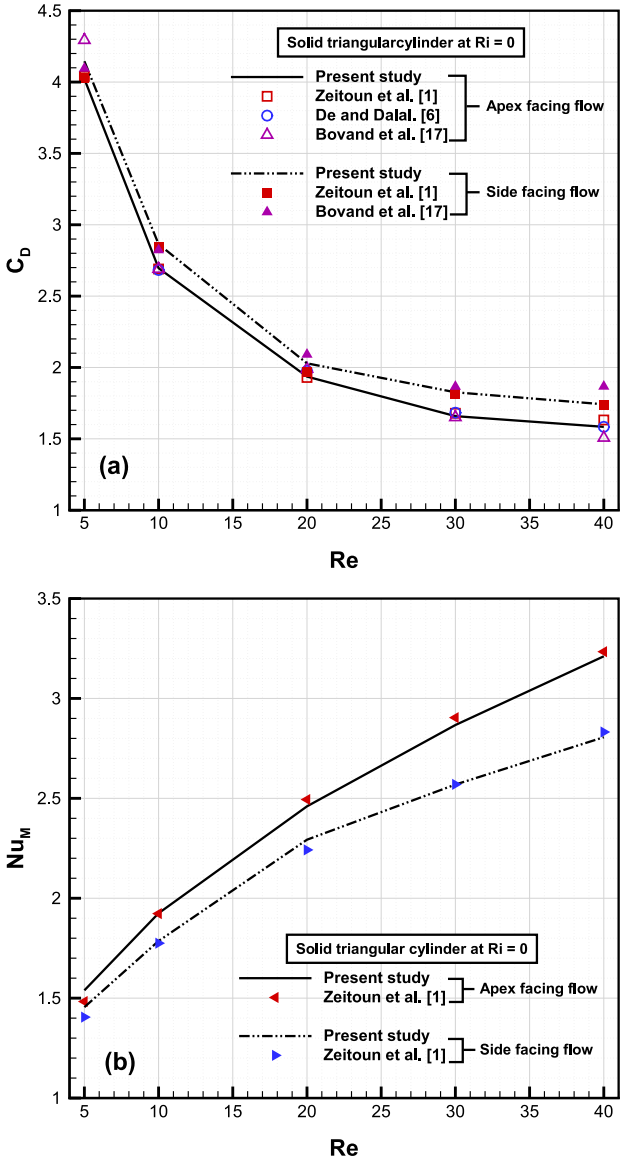

Fig. 2. Comparison of impermeable triangular cylinder results from present code with literature for $Pr = 0.71$ (a) drag coefficient (C_D) and (b) mean Nusselt number (Nu_M).

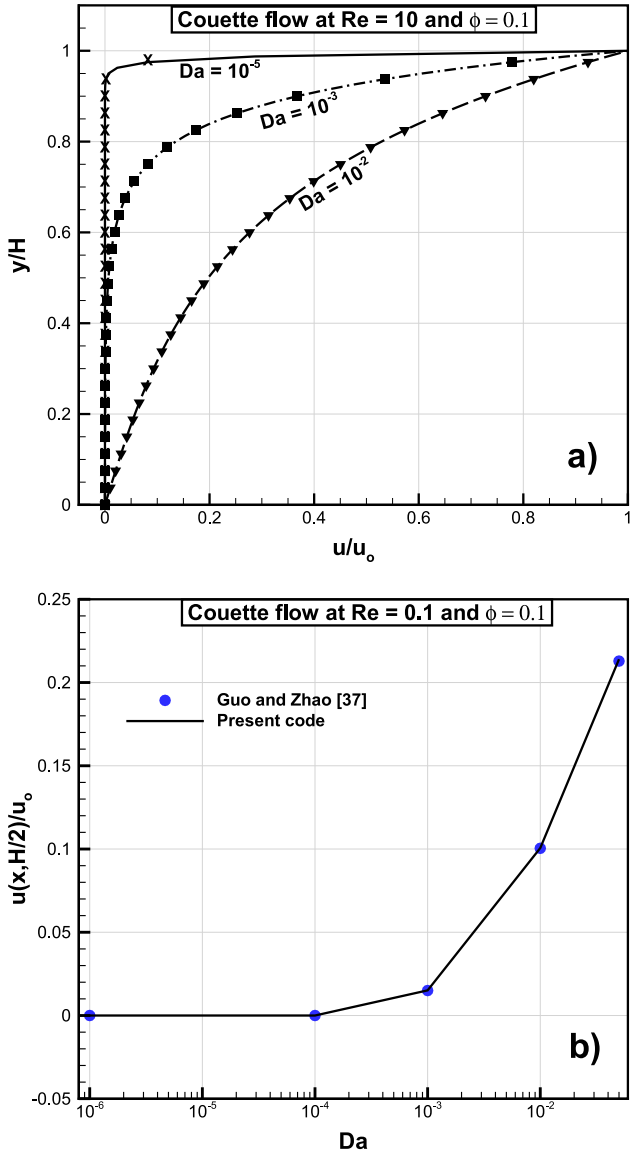

Fig. 3. (a) Velocity profiles of the Couette flow (cavity filled with porous medium) at $Re = 10$ for different values of Da. Symbols represent the results from the present code, and the lines indicate analytical solution. (b) Velocity at the midway of the centre against Darcy number at $Re = 0.1$.

If we compare the streamline contours around apex and side facing triangular configurations, at $Da = 10^{-4}$ and 10^{-3}, the flow resistance is more in the case of side facing flow for all values of Re. This is due to the fact that the windward surface of this configuration has a larger porous zone. But in case of apex facing flow, porous zone diverges equally from apex point of the cylinder and therefore, the resistance offered by porous medium reduces. One can also notice that the separation point moves forward from the corners of side facing flow due to the increment of non-dimensional permeability. At $Da = 10^{-2}$, both triangular bodies are not offering any resistance to the fluid flow. When the porous body is brought under buoyancy (*i.e.* at $Ri = 0.5$ and 1), more fluid sticks over the cylinder surface due to the reduction of pressure over it. Therefore, buoyancy induces more fluid to enter into porous zone. It can be seen from Fig. 4 that while increasing Ri values, the recirculation eddies that form behind the cylinder reduces and further, it also reduces while increasing Darcy number. Additionally, the wake detaches from the leeward surface of apex facing triangular cylinder at $Da = 10^{-3}$. Interestingly, at $Ri = 1$ and $Re = 40$, there is no wake formation behind the side facing flow triangular configuration. In the case of apex facing flow, due to thinning of viscous layer by the slant edges, fluid accelerates more and thus, the wake forms downstream of the porous body even at higher Ri. Hence, it is clear that the streamline patterns are a function of Re, Da, forebody and afterbody shapes and also buoyancy condition.

4.1.2. Vorticity pattern

To impart further insight on fluid flow behaviour near to the permeable triangular cylinder, the vorticity contours are presented in Fig. 5. The dotted and solid line represents the negative and positive values of vorticity. It is a well-known fact that the intensity of local rotation of fluid increases with Reynolds number due to the depletion of viscous layer. The presence of viscous layer reduces the movement of fluid, which reduces the strength of vorticity at lower Re values. Meanwhile, this intensity reduces with the increase of buoyancy level. The prominent viscous layer at higher Richardson number is the cause of such reduction. The same observation can be seen in Fig. 5 for all values of Da. Furthermore, a rich permeable cylinder shortens the local recirculation. While

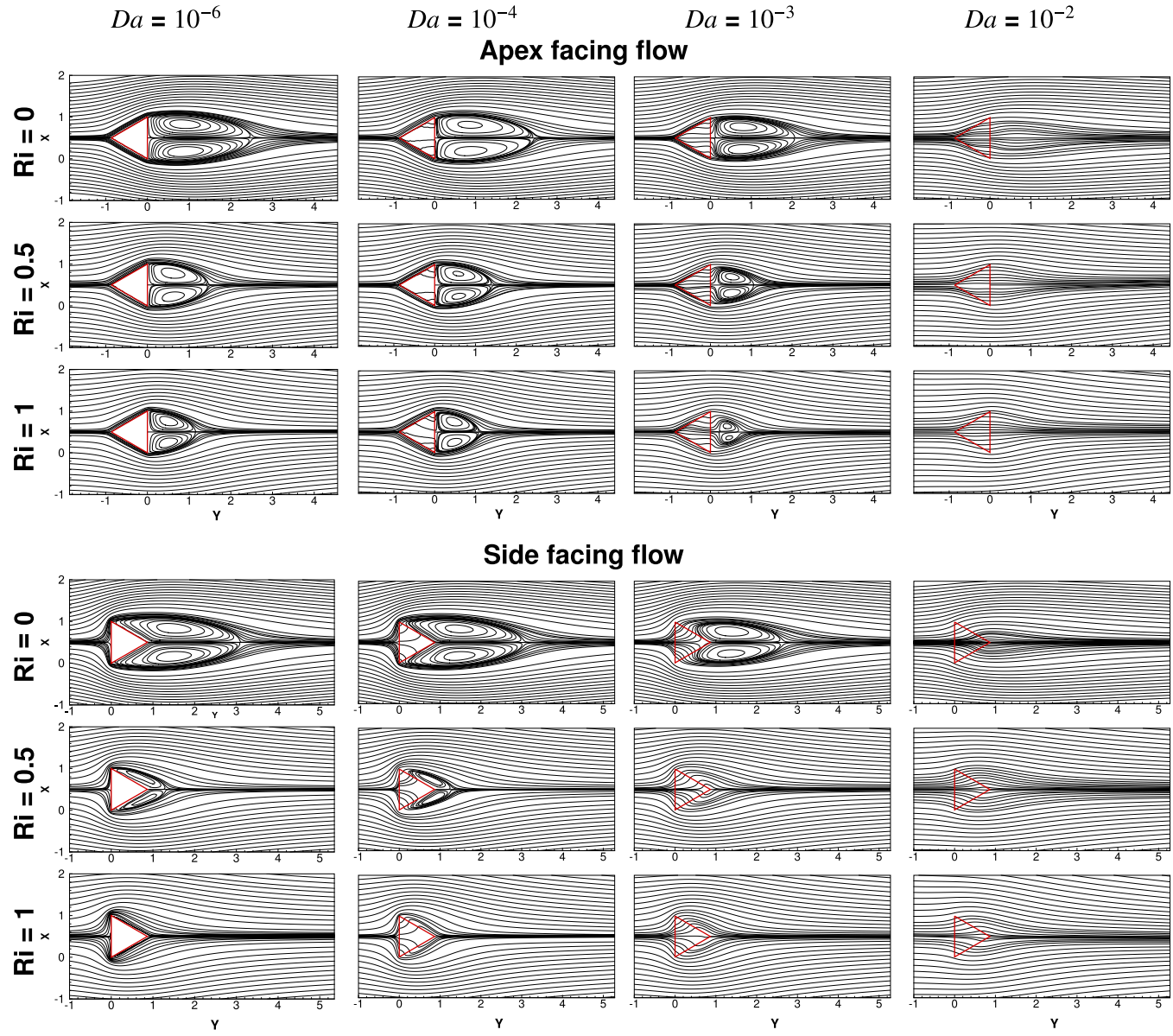

Fig. 4. Streamlines at $Re = 40$ and $Ri = 0, 0.5$ and 1 for various Darcy numbers for the flow around and through the porous triangular cylinder.

increasing *Da* levels, the vortices are seen to diffuse into the porous cylinder, due to less resistance offered to the flow. Also, diffused fluid is decelerated by the viscous force that exists in the permeable cylinder. Hence, the strength of vorticity reduces with the increment in *Da* values. Such diffusion is found to be more at higher values of *Ri* for a constant value of *Da*. In addition, the slant surfaces of apex facing flow configuration allows more fluid to diffuse into it than side facing triangular configuration. Forebody shape of the two triangular configurations render variations in vorticity length. For example, at $Ri = 0$ and $Da = 10^{-3}$, the vorticity length of apex facing triangular configuration is lesser than that of the other. Thus, a cylinder with higher *Da* under aiding buoyancy condition, provides lesser stability issues compared to the impermeable case; the forebody plays an important role on vorticity pattern.

4.1.3. Drag coefficient (C_D)

To deliver quantitative effects of Reynolds number, permeability and forebody shape on the flow behaviour around and through porous triangular cylinder, the coefficient of drag (C_D) variation have been presented for apex facing and side facing flow configurations in Fig. 6(*a*) and (*b*). The drag force is evaluated by momentum exchange method, in which the exchange of momentum between two opposing directions of the neighbouring lattices of cylinder surface are used to determine the forces acting on the cylinder [61]. It is obvious that the drag force decreases with the increment in Reynolds number due to thinning of viscous layer around the cylinder. The drag coefficient of permeable triangular cylinder also decreases with the increase in *Re*. However, due to the reduction of fluid resistance at higher permeability levels, the pressure difference between windward and leeward surfaces reduces. As a result of this, C_D decreases monotonously while increasing with Darcy number and this effect is found to be common for both, apex and side facing flow configurations. Furthermore, while increasing *Ri*, the drag coefficient jumps to a higher value for constant *Re* and *Da* value. Under aiding buoyancy condition, viscous layer over cylinder surface becomes thick and hence, overall drag force increases substantially with the increment in Richardson number. At $Ri = 0$, C_D value of apex facing flow is lower than that of side facing flow configuration. As discussed earlier, the slant forebody of apex facing flow reduces the viscous layer thickness and therefore,

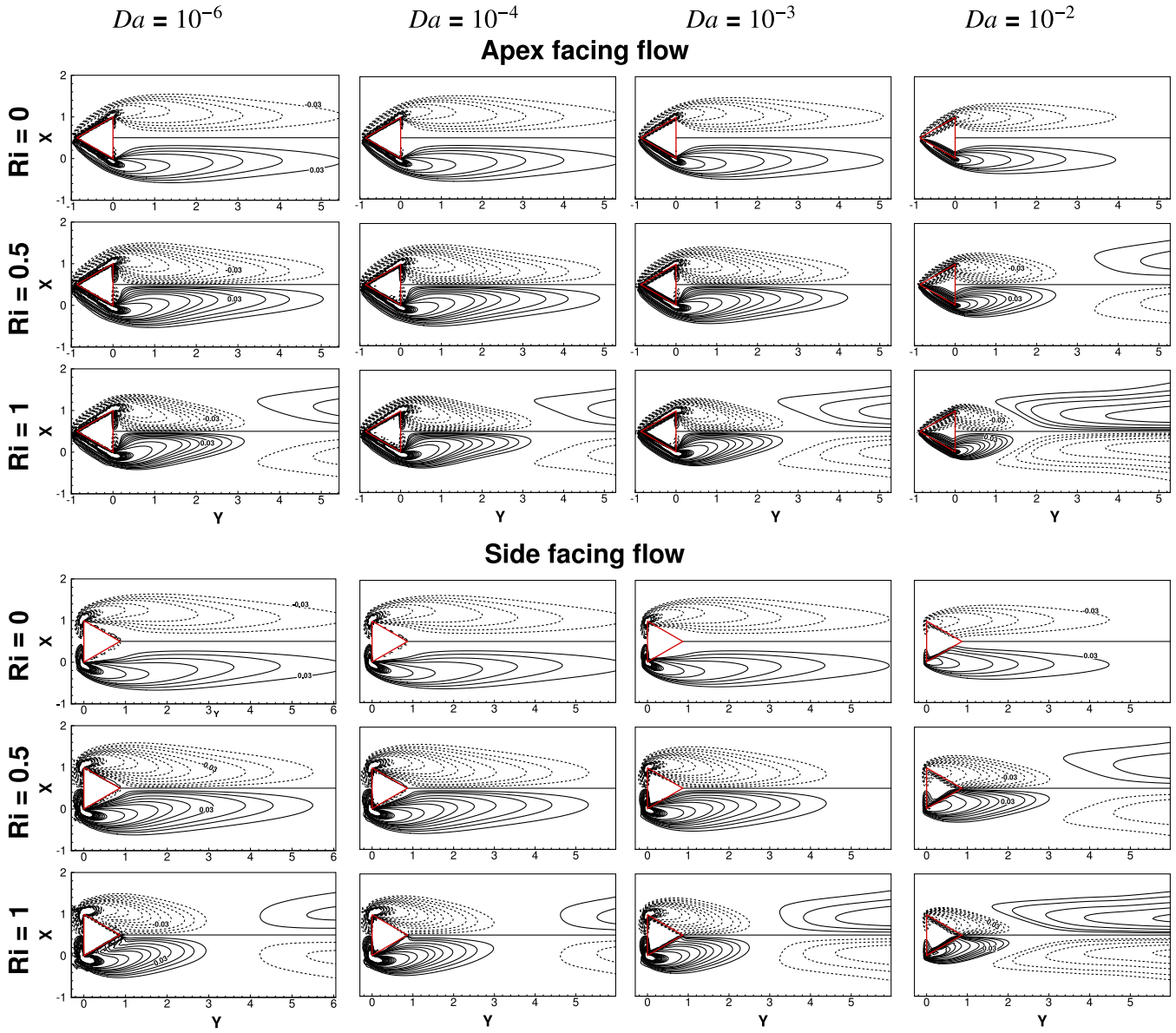

Fig. 5. Vorticity contours at $Re = 40$ and $Ri = 0, 0.5$ and 1 for various Darcy numbers for the flow around and through the porous triangular cylinder.

it experiences lesser drag force. Interestingly, at higher *Ri* values, it is observed that the drag coefficient of side facing cylinder is slightly lower than that of the apex facing flow for all values of *Da*. Additionally, we have also compared the drag coefficient values of solid square cylinder with triangular cylinders at different convection rates and aiding buoyancy condition which is shown in Fig. 7. For all values of *Re* and/or *Ri*, the drag coefficient of square cylinder is higher than that of triangular configurations. In the absence of buoyancy, the drag coefficient value of side facing flow lies between the square and apex facing flow configurations. However, while increasing *Ri* from 0 to 0.5, the drag force of apex facing flow configuration is marginally higher than side facing flow case. At *Ri* = 1, one can observe a notable difference in drag coefficient between side and apex facing flow configurations.

4.1.4. Wake length variation (L_r)

It is evident from streamline contours, the fluid separates at corners of flat edges of the cylinder and then it attaches at downstream, for both triangular orientations. In the present analysis, streamwise distance from the separation point to the reattachment point is denoted as wake length (L_r). It should be noted that the flow separates from the edge *BC* and *QR* for apex and side facing flow configurations, respectively. Fig. 8(*a*) and (*b*) graphically illustrates the variation of wake length with Reynolds number at $Da = 10^{-6}, 10^{-4}, 10^{-3}$ and at *Ri* = 0, 0.5 and 1. It is a well-known fact that, while increasing *Re*, the inertial force increases which depletes viscous layer over cylinder. As a result of this, wake length increases with the increment in *Re*. Further, while increasing non-dimensional permeability of porous triangular cylinder, the wake length reduces marginally. Change in separation point location due to fluid penetration is the cause for such wake length reduction. At $Da = 10^{-4}$, the wake length reduction is found to be very less with respect to $Da = 10^{-6}$. It should be noted that at $Da = 10^{-2}$, there is no wake formation behind cylinder. In the case of side facing flow triangular cylinder, recirculation eddies forms only when $Re > 10$ and the same has been reported in earlier stud-

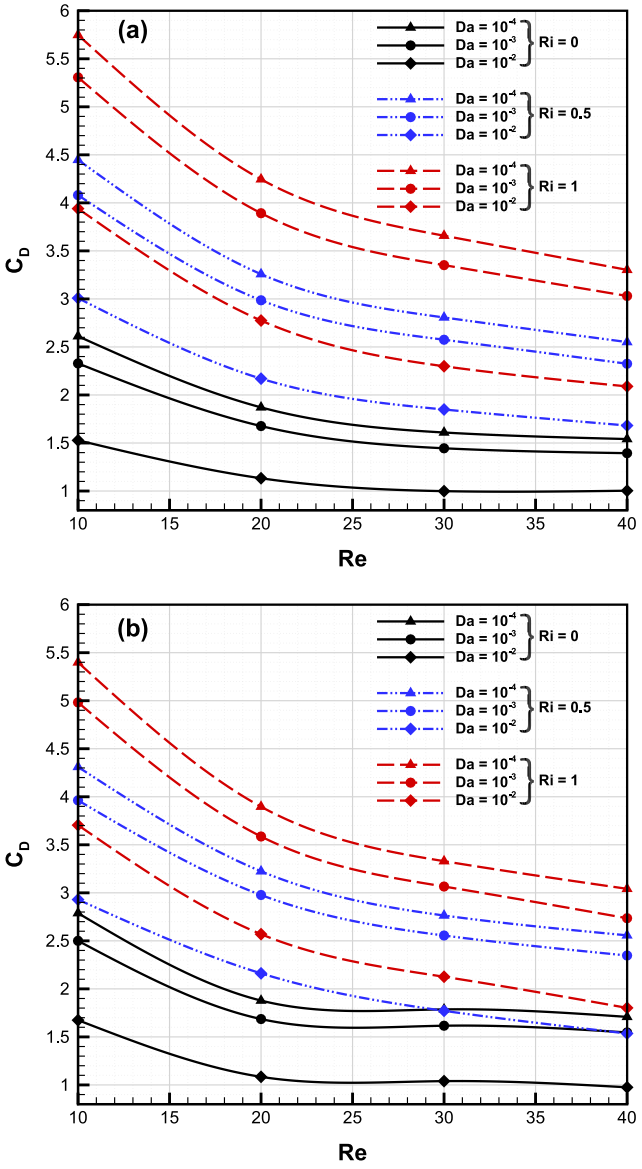

Fig. 6. Variation of drag coefficient (C_D) with Re for different values of Ri and Da for the flow through and around a porous triangular cylinder. (a) apex facing flow (b) side facing flow.

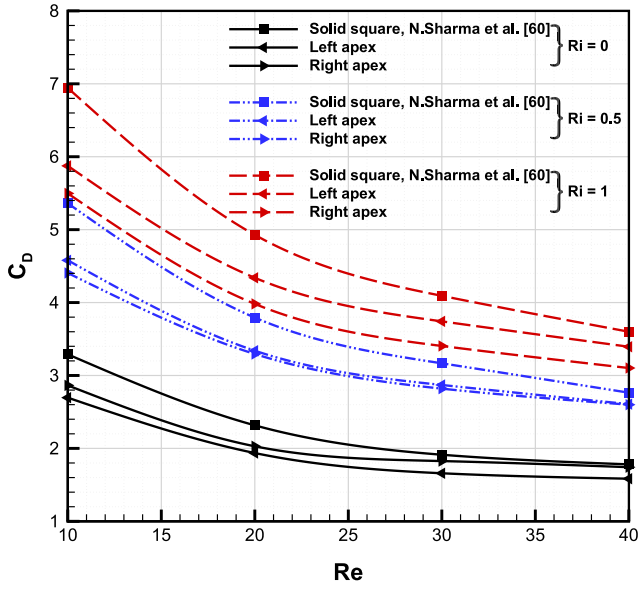

Fig. 7. Comparison of drag coefficient (C_D) values of apex facing flow, side facing flow triangular cylinder with square cylinder under different buoyancy levels at $10 \leqslant Re \leq 40$ and $Da = 10^{-6}$.

ies [5–8,11]. The aiding buoyancy produces thick viscous layer over triangular body and therefore, more fluid particles stick over it. Due to this, fluid looses its inertial effects and thus, the reattachment occurs earlier than that of cylinder without buoyancy. Hence, wake length reduces with the increment in Ri values for a constant value of Re and Da. The compression of wake length is found to be predominant while Richardson number shifts from 0 to 0.5. It is seen that there is no wake formation at $Ri = 1$, $Da = 10^{-3}$ and $Re < 7$ for the apex facing flow triangular configuration. Also, no recirculation eddies are seen for the case of side facing flow at all values of Re and at $Ri = 1$. In addition, at $Ri = 0.5$, for side facing flow configuration one can observe the wake pattern and depletion of same at $Da = 10^{-3}$ from Fig. 4. Even under the influence of buoyancy, the flow separates for the apex facing flow, inpsite of increased viscous layer thickness. This occurrence is because of the slant forebody edges, which accelerates the flow as it comes. For the side facing flow configuration, at higher Richardson number, the thick viscous layer developing on the aftbody slant edges deaccelerates the flow at corners of the forebody edge, resulting in a fully-attached flow even at higher convection rates. Hence, it can be concluded that the buoyancy effect is significant and non-dimensional permeability effect is marginal on the reduction as well as suppression of wake. Further we have used non-linear regression to express the relationship between wake length and Re, Da and Ri, it can be written as

$$L_r = -0.002 \times ln(Re)^{2.939}(1+Ri)^{-1.589}[ln(Da) - 13.905] + 0.302 \quad \text{apex facing} \tag{29}$$

$$L_r = -0.002 \times ln(Re)^{2.392}(1+Ri)^{-1.466}[ln(Da) - 57.065] + 0.851 \quad \text{side facing} \tag{30}$$

The correlation coefficient values (R^2) of above expressions are found to be 0.98. It is to be noted that in the case of side facing configuration, since there is no recirculation at $Ri = 1$, the same Richardson number is not considered while obtaining the correlation.

4.2. Heat transfer characteristics

A detailed discussion on the effects of Reynolds number (Re), Darcy number (Da), Richardson number (Ri) and forebody shape of triangular configuration on heat transfer characteristics is discussed in this section. The results are visualised in terms of isotherms, compared through Enhancement ratios (E) and quantified in terms of mean Nusselt number values.

4.2.1. Isotherms

Fig. 9 exhibits the influence of Darcy number and aiding buoyancy level on temperature distribution near the porous triangular zone at $Re = 40$ and $Pr = 0.71$ for apex and side facing triangular cylinder configurations. It can be seen that thermal patterns around the porous body can be greatly altered by aforementioned parameters. The effects of Re variation on isotherms around solid triangular cylinder (both apex and side facing triangular configuration) have been reported by various researchers [1,10–15,17,19]. It is seen that while increasing Re, the isotherm patterns spread along the streamwise direction with a subsequent reduction in lateral width. Due to such convective dominance, the thermal boundary

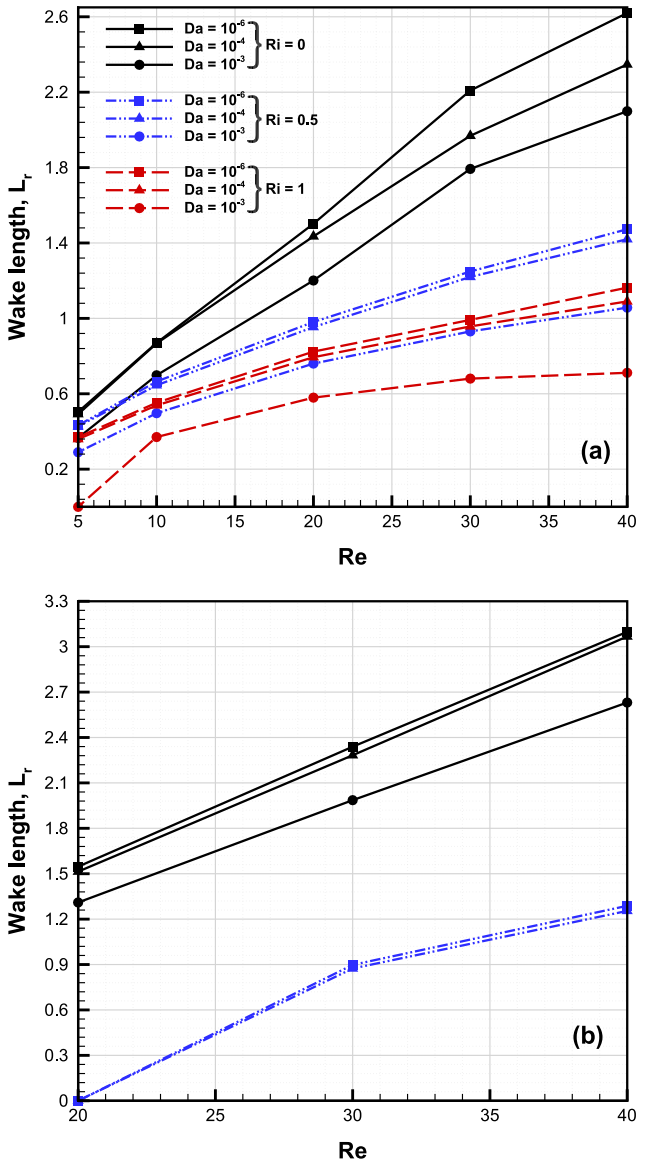

Fig. 8. Wake length (L_r) variations at different *Re*, Darcy number ($10^{-6} \leqslant Da \leqslant 10^{-2}$) and Richardson number ($Ri = 0$, 0.5 and 1) for flow around and through triangular cylinder (a) apex facing flow (b) side facing flow.

layer around the cylinder reduces, which results in a linear augmentation of heat transfer. We further explore the influence of *Da* and *Ri* on thermal behaviour of the cylinder at a constant value of *Re*. It can be visualized from Fig. 9 that the thermal plume stretches more in the downstream direction, while increasing the non-dimensional permeability of cylinder. The lateral width reduction of isotherm at higher values of *Da* is evident for the increment of thermal gradient near to the body. Thus, heat transfer rate can be escalated by increasing Darcy number of the permeable triangular cylinder. It should be noted that the thermal gradient is more at frontal surfaces of the cylinder (for both apex and side facing to flow configuration) and the same is found to be less at leeward surfaces while increasing non-dimensional permeability. A rich permeable body allows more fluid and hence, heat is also being convected through the cylinder. As a result of this, the thermal boundary layer on leeward surfaces becomes thick with the increment in *Da*. Turning to the effects of buoyancy, the isotherm patterns are found to cluster more over the cylinder while increasing *Ri* value from 0 to 0.5. At $Da = 10^{-6}$ and $Ri = 0.5$, the thermal pattern becomes narrower than forced convection case (*i.e.* $Ri = 0$) and further increment in *Da* increases its lateral width scarcely. This is due to the decrement of thermal gradient across the leeward surface. Any further increment in *Ri*, depletes thermal boundary layer over the cylinder. This discussion is common for both apex and side facing flow configurations of permeable triangular cylinder. In Fig. 9 we have also mentioned an isotherm contour value of 0.95 in order to understand the influence of Darcy number, Richardson number as well as the configuration of porous triangular cylinder. For the case of apex facing configuration, this isotherm value is more at edge *BC*, and the shape of this contour turns to triangular from semi-circular shape while increasing *Ri*. However, in the case of side facing configuration, this non-dimensional isothermal value is observed near the edges *PQ* and *QR*.

4.2.2. Heat transfer enhancement along the cylinder surface

Fig. 10(a)–(d) depict the representative variation of the heat transfer enhancement ratio due to buoyancy on each surface of the permeable triangular shaped cylinder for different values of *Re* and *Da*. In Section 4.2.1, we have discussed the effects of Darcy number on the variation of temperature distribution. It was seen that the temperature gradient at rear or leeward surfaces of cylinder decreases when the cylinder turns to be more permeable. To further impart knowledge of *Ri* variation on heat transfer characteristics, heat transfer enhancement ratio (E) due to buoyancy effects is presented for each surface of the cylinder; and it is evaluated from Eq. (27). In the case of apex facing flow triangular cylinder, the front slant faces (edge *AB* & *AC*) are in direct contact with fluid and hence, it produces thermal enrichment than the edge *BC*. Also, in the case of side facing flow configuration, the heat dissipation of edge *RQ* is higher than other two slant edges. Fig. 10(a) indicates that the increment of *Re* reduces enhancement ratio for $Da \leqslant 10^{-4}$. This is due to the fact that Richardson number is indirectly proportional to *Re* (*i.e.* $Ri = Gr/Re^2$). However, the enhancement ratio increases with further increment in Darcy number and this is found to be prominent at $Da = 10^{-2}$. It should also be noted that the value of E of a highly permeable cylinder reduces at very low values of *Re*. One can notice that the heat transfer enhancement ratio at edge *BC* is higher than that of other edges of the cylinder at this Darcy number value. In addition, the enhancement ratio reduces for $Da \leqslant 10^{-3}$ with the increment in *Re*. In the case of side facing flow, heat transfer enhancement ratio trend of edge *RQ* is same as that for the edges *AB* and *AC*. Further, the thermal dissipation of slant edges of side facing flow configuration increases with *Re* up to 30 and then it falls due to the dominance of convection.

4.2.3. Mean Nusselt number (Nu_M)

The effects of non-dimensional permeability on mean Nusselt number at different values of Reynolds number and Richardson number are illustrated in Figs. 11 and 12 for apex and side facing flow configurations of permeable triangular cylinder, respectively. It is clear that Nu_M increases linearly with the increase of *Re* at all levels of non-dimensional permeability and buoyancy levels. Although, the leeward surfaces of both triangular configurations produce diverse effects on heat transfer performance with *Da* increment, the mean Nusselt number increases with the increase of *Da* values. However, there is no significant variation in mean Nusselt number with *Da* at $Re \leqslant 5$; less fluid penetration into the cylinder and the dominant viscous forces inside the porous body are the causes for this. At higher *Re*, the effects of *Da* on Nu_M is prominent; the rich fluid penetration, depletion of viscous and increment in internal forces inside the porous zone is the cause of such heat transfer enhancement. Also, the heat transfer variation

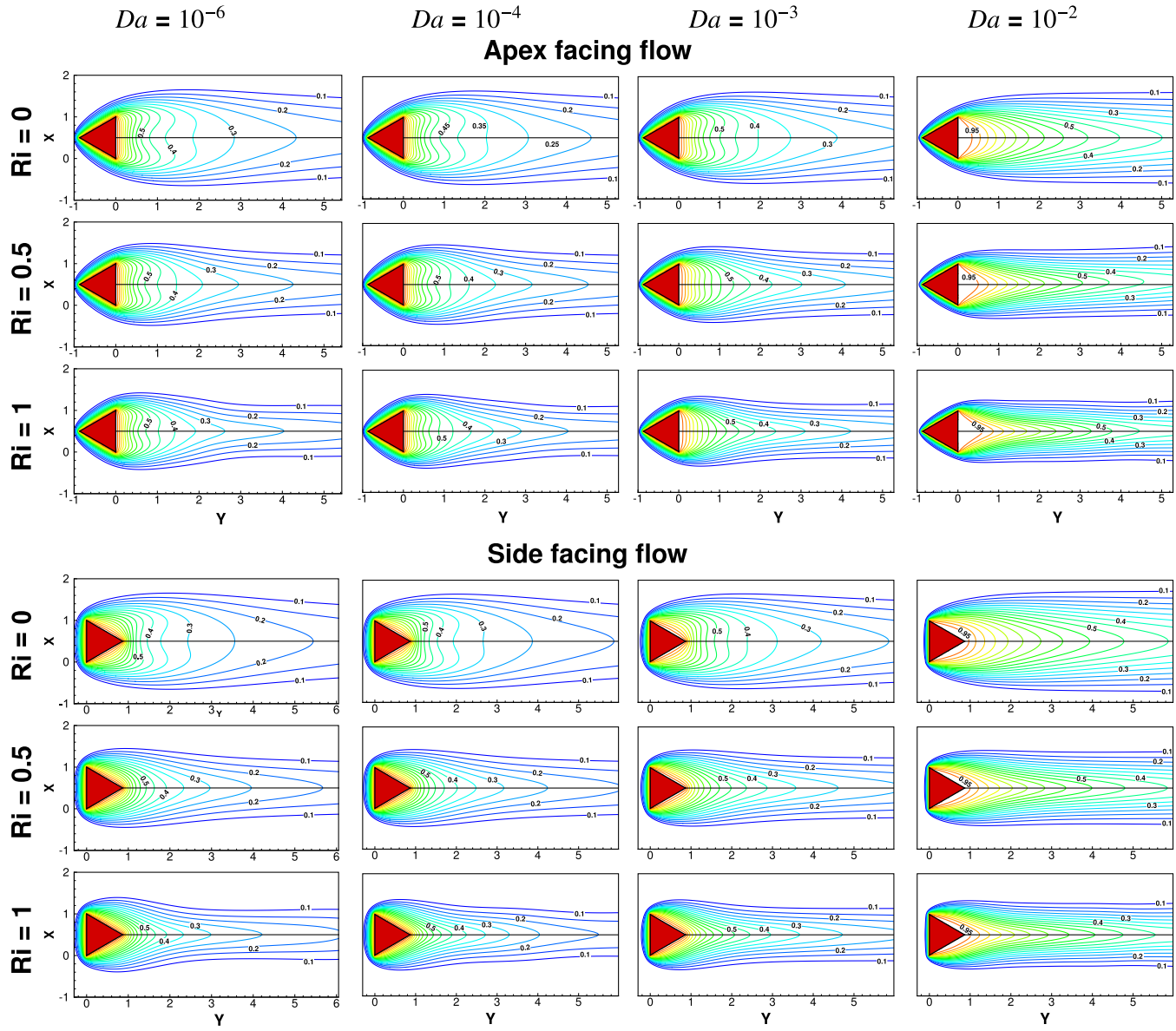

Fig. 9. Isotherms at $Re = 40$ and $Ri = 0, 0.5$ and 1 for various Darcy numbers for the flow around and through the porous triangular cylinder.

between $Da = 10^{-6}$ and 10^{-4} is found to be marginal. In addition, Nu_M values at $Da = 10^{-6}$ is matching with those values of impermeable cylinder. Thus, at this non-dimensional permeability level, porous triangular cylinder behaves as a solid body. The effects of Darcy number on heat dissipation is further escalated through buoyancy. For example, the percentage enhancement in mean Nusselt number at $Re = 30$, $Da = 10^{-4}$ and $Ri = 0$, 0.5 and 1 is 2.35%, 2.56% and 2.82%, respectively, compared to solid cylinder for apex facing flow triangular configuration. Whereas, for the same flow parameters, the side facing flow triangular cylinder have shown the enhancement of 2.43%, 2.5% and, 2.61%. Further, we have compared the Nusselt number value of solid square cylinder with two triangular configurations embraced in this study at $10 \leqslant Re \leqslant 40$ and $Ri = 0$, 0.5 and 1. Fig. 13 indicates that irrespective of Re and Ri, the apex facing flow triangular configurations deliver maximum heat transfer followed by side flow and square cylinder. This is due to the fact that the apex facing configuration has two windward surfaces in slanting position. For the cases of side facing triangular configuration as well as square cylinder, only one edge comes in the direct contact of fluid. Same trend of Nu_M is also seen while comparing it with the different values of Da. Therefore, it can be concluded that the heat dissipation is augmented by increasing Da, Ri and also by keeping apex of the triangular cylinder to face flow. The cumulative effects of non-dimensional permeability and buoyancy level further improves the mean Nusselt number.

Furthermore, from the engineering application viewpoint, simple expressions are presented for Nusselt number as a function of Re and Da. The constants (a_1, a_2, a_3 and a_4) of this expression for different values of Ri and configuration are shown in Table 5. The correlation coefficient values (R^2) are found to be not less than 0.991. It should be noted that R^2 gives the fit relationship between numerically observed values and data derived from the expression. For instance, if R^2 is equal to 1, then all values are falls inside the trend line obtained from the equation. The simple expression can be written as

$$Nu_M = a_1 Re^{a_2}\left(\sqrt{Da} + a_3\right) + a_4 \tag{31}$$

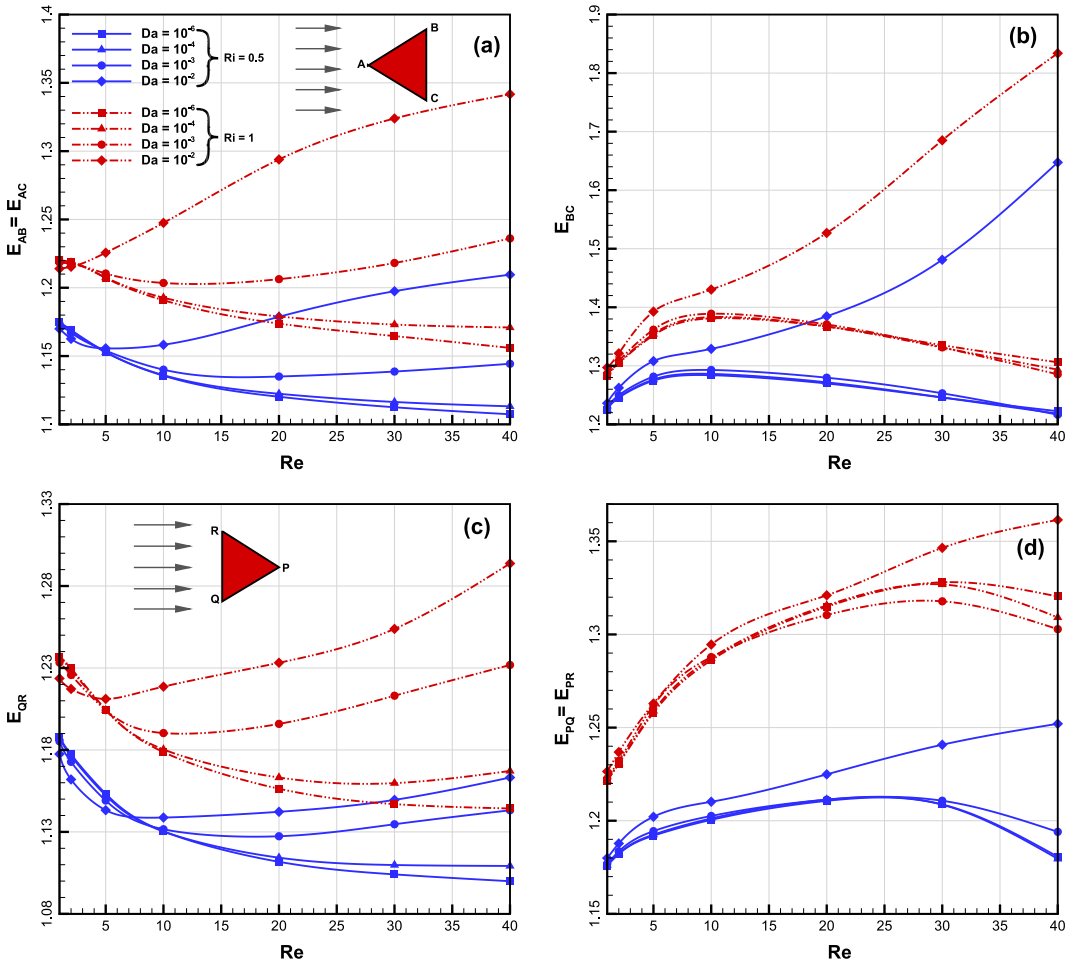

Fig. 10. Effect of Richardson number on heat transfer enhancement ratio at different Reynolds number and Darcy number on (a) slant faces of apex facing flow (b) flat face of apex facing flow and (c) flat face of side facing flow (d) slant faces of side facing flow of the heated permeable triangular cylinder in an unbounded domain.

A common expression for different values of Richardson number with R^2 value of 0.989 is also formulated for apex and side facing triangular cylinders. The expressions are as follows:

$$Nu_M = 0.871Re^{0.811}(1+Ri)^{0.537}\left(\sqrt{Da}+0.104\right)+1.305 \quad \text{(apex facing)} \tag{32}$$

$$Nu_M = 0.99Re^{0.8}(1+Ri)^{0.539}\left(\sqrt{Da}+(0.00782)\right)+1.376 \quad \text{(side facing)} \tag{33}$$

5. Concluding remarks

The flow and heat transfer characteristics of an equilateral permeable triangular cylinder placed in a uniform flow have been numerically examined under the aiding buoyancy condition. The influence of Reynolds number, Darcy number and Richardson number on hydrodynamic and thermal behaviour of apex and side facing triangular cylinder configurations have been investigated by lattice Boltzmann technique. In order to obtain porous body characteristics and buoyancy effects, Darcy-Forchheimer and Boussinesq terms are coupled with the BGK collision equation. The important outcomes of this study can be highlighted as follows:

1. Both apex and side facing triangular configurations, imitate solid body characteristics for all values of *Re* at $Da = 10^{-6}$. As *Da* increases, fluid starts to enter into cylinder with different deviation levels. The flow deviation produced by apex facing triangular cylinder is lesser than that of side facing flow. This is due to less viscous forces acting on the forebody of former configuration. At $Da = 10^{-2}$, almost all fluid penetrates into the permeable body and hence, no wake formation is observed.
2. Strength of vorticity in the vicinity of the permeable triangular cylinder can be greatly altered by varying *Da* and *Ri*. Fluid diffuses into the cylinder while triangular cylinder becomes permeable and this effect is prominent at higher *Da* and *Ri*. Due to the flat windward surface of side facing triangular cylinder, the local rotation of fluid is found to be more.
3. The excess viscous forces offered by buoyancy is the cause for substantial increment and decrement of drag coefficient and recirculation length values, respectively. However, more permeable triangular body experiences less drag value with short eddies. Flow separation and wake stagnation points move forward while increasing *Da*. The side facing triangular cylinder configuration exerts less drag force than the apex facing cylinder only at higher *Ri* (*i.e.* $Ri > 0$).
4. Thermal gradient reduction is evident from the lateral width reduction of isotherms at higher non-dimensional permeability. Also, increment in *Da* produces diverse effects on heat transfer performances at the leeward surface of permeable triangular body. Further, thermal plume turns to be narrow under the aiding buoyancy condition.

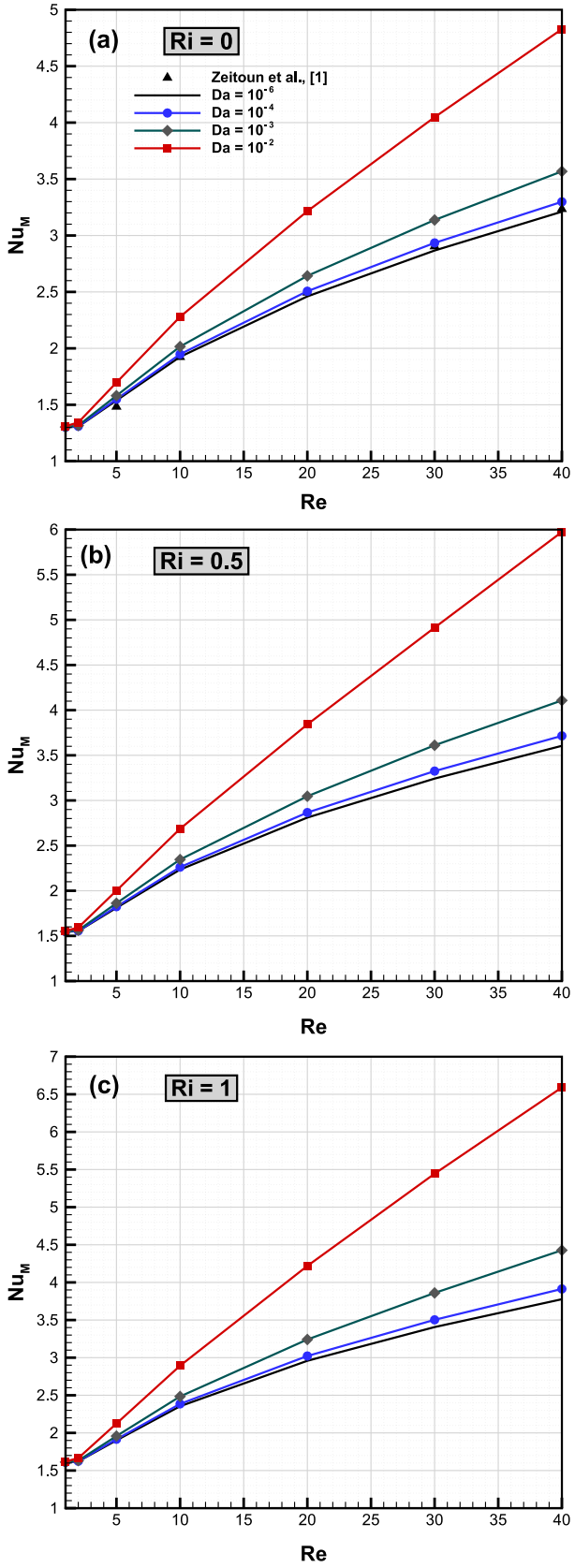

Fig. 11. Effect of Darcy number on mean Nusselt number (Nu_M) at different Reynolds numbers (a) $Ri = 0$; (b) $Ri = 0.5$ and (c) $Ri = 1$ for flow through and around the permeable triangular cylinder apex facing flow.

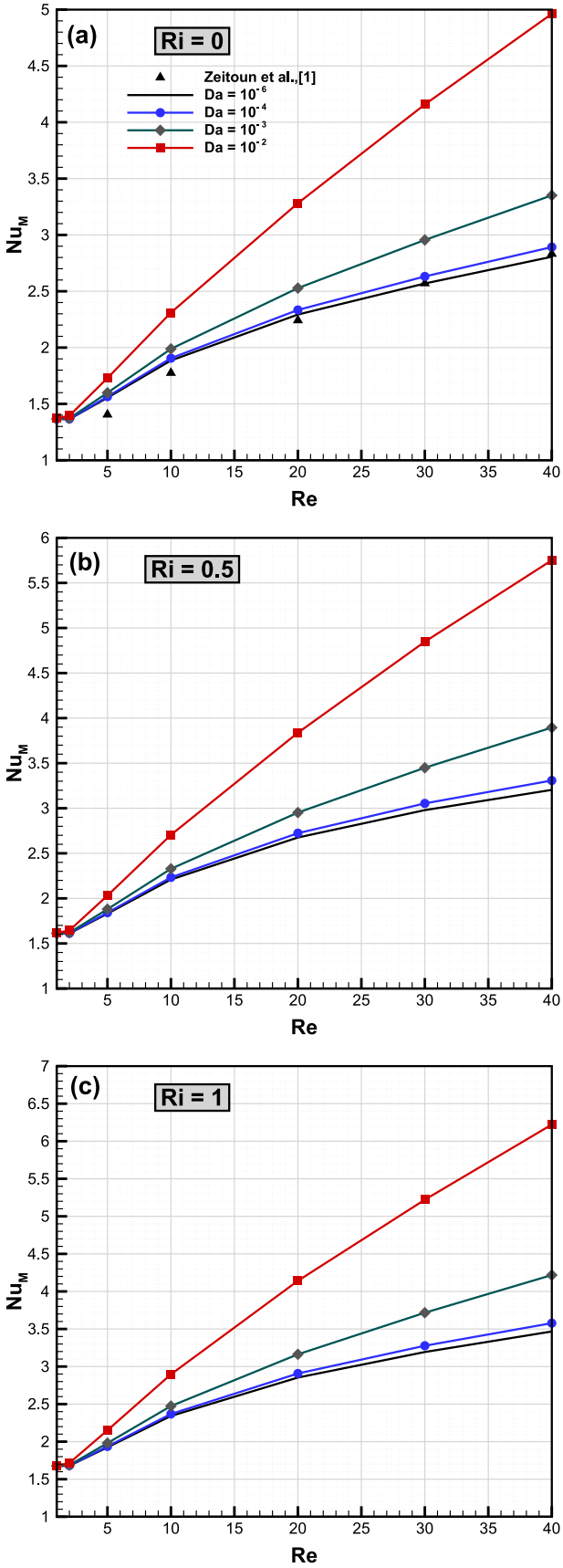

Fig. 12. Effect of Darcy number on mean Nusselt number (Nu_M) at different Reynolds numbers (a) $Ri = 0$; (b) $Ri = 0.5$ and (c) $Ri = 1$ for flow through and around the permeable triangular cylinder side facing flow.

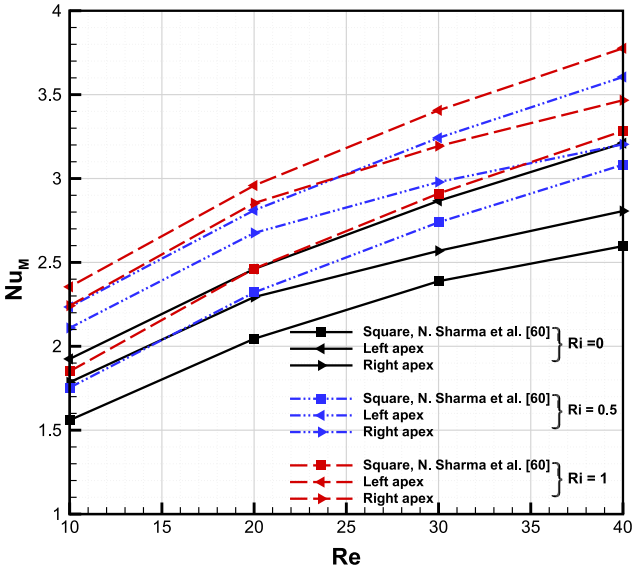

Fig. 13. Comparison of mean Nusselt number (Nu_M) values of apex facing flow, side facing flow triangular cylinder with square cylinder under different buoyancy levels at $10 \leqslant Re \leq 40$ and $Da = 10^{-6}$.

Table 5
Constants of correlation expression (Eq. (31)) for Mean Nusselt number at different values of *Ri*.

S. No.	Configuration	*Ri*	a_1	a_2	a_3	a_4	R^2
1	Apex facing flow	0	0.809	0.796	0.137	1.129	0.995
2		0.5	0.971	0.847	0.1	1.397	0.993
3		1	1.129	0.859	0.087	1.462	0.993
4	Side facing flow	0	0.896	0.854	0.075	1.246	0.993
5		0.5	1.074	0.847	0.072	1.487	0.991
6		1	1.201	0.838	0.075	1.533	0.992

R^2 – Correlation coefficient.

5. Heat transfer enhancement produced by buoyancy decreases at the windward surfaces of body with an increment in buoyancy levels for $Da \leqslant 10^{-4}$; intensity of the same phenomena increases with further increment in *Da*. Heat transfer enrichment is evident from the mean Nusselt number increment with *Da* and *Ri*. However, at low *Re* there is significant variation in heat dissipation with aforementioned parameters. Rich thermal performances are observed for apex facing triangular configuration for all values of *Re*, non-dimensional permeability levels, and buoyancy conditions in comparison with side facing cylinder.

Hence, it is clear that the flow and thermal behaviour can be regulated by tuning permeability, buoyancy condition and configuration of permeable body for real life applications. The thermal behaviour can be further intensified by reducing channel height and changing the buoyancy orientations [31]. Therefore, a detailed investigation on thermal characteristics around a permeable triangular body with different configurations in a confined channel under different buoyancy orientation can be carried out in future.

Conflict of interest

The authors declare that there is no conflict of interests.

Acknowledgement

One of the authors, S. Dhinakaran, gratefully acknowledges the fund received from Council of Scientific & Industrial Research (CSIR), Government of India, through a project grant (Project Reference No. 22(0642)/13/EMR-II) for carrying out this work.

References

[1] O. Zeitoun, M. Ali, A. Nuhait, Convective heat transfer around a triangular cylinder in an air cross flow, Int. J. Therm. Sci. 50 (9) (2011) 1685–1697.
[2] S. Dhinakaran, J. Ponmozhi, Heat transfer from a permeable square cylinder to a flowing fluid, Energy Convers. Manage. 52 (5) (2011) 2170–2182.
[3] S. Rashidi, A. Tamayol, M.S. Valipour, N. Shokri, Fluid flow and forced convection heat transfer around a solid cylinder wrapped with a porous ring, Int. J. Heat Mass Transf. 63 (2013) 91–100.
[4] S. Rashidi, M. Bovand, I. Pop, M.S. Valipour, Numerical simulation of forced convective heat transfer past a square diamond-shaped porous cylinder, Transp. Porous Media 102 (2) (2014) 207–225.
[5] Y. Bao, D. Zhou, Y.-J. Zhao, A two-step Taylor-characteristic-based Galerkin method for incompressible flows and its application to flow over triangular cylinder with different incidence angles, Int. J. Numer. Meth. Fluids (2009) 1181–1208.
[6] A.K. De, A. Dalal, Numerical simulation of unconfined flow past a triangular cylinder, Int. J. Numer. Meth. Fluids 52 (7) (2006) 801–821.
[7] J. Tu, D. Zhou, Y. Bao, Z. Han, R. Li, Flow characteristics and flow-induced forces of a stationary and rotating triangular cylinder with different incidence angles at low Reynolds numbers, J. Fluids Struct. 45 (2014) 107–123.
[8] A.K. Dhiman, S. Kumar, Non-Newtonian power-law flow across a confined triangular bluff body in a channel, Kor. J. Chem. Eng. 30 (1) (2013) 33–44.
[9] A.K. Tiwari, R.P. Chhabra, Effect of orientation on the steady laminar free convection heat transfer in power-law fluids from a heated triangular cylinder, Numer. Heat Transf. Part A: Appl. 65 (8) (2014) 780–801.
[10] S. Srikanth, A. Dhiman, S. Bijjam, Confined flow and heat transfer across a triangular cylinder in a channel, Int. J. Therm. Sci. 49 (11) (2010) 2191–2200.
[11] A.K. De, A. Dalal, Numerical study of laminar forced convection fluid flow and heat transfer from a triangular cylinder placed in a channel, J. Heat Transf. 129 (5) (2007) 646.
[12] D. Chatterjee, B. Mondal, Forced convection heat transfer from an equilateral triangular cylinder at low Reynolds numbers, Heat Mass Transf. 48 (9) (2012) 1575–1587.
[13] A. Dhiman, R. Shyam, Unsteady heat transfer from an equilateral triangular cylinder in the unconfined flow regime, ISRN Mech. Eng. 2011 (2011) 1–13.
[14] A. Prhashanna, A.K. Sahu, R. Chhabra, Flow of power-law fluids past an equilateral triangular cylinder: momentum and heat transfer characteristics, Int. J. Therm. Sci. 50 (10) (2011) 2027–2041.
[15] A. Bose, N. Nirmalkar, R.P. Chhabra, Forced convection from a heated equilateral triangular cylinder in Bingham plastic fluids, Numer. Heat Transf. Part A: Appl. 66 (1) (2014) 107–129.
[16] M. Farhadi, K. Sedighi, A.M. Korayem, Effect of wall proximity on forced convection in a plane channel with a built-in triangular cylinder, Int. J. Therm. Sci. 49 (6) (2010) 1010–1018.
[17] M. Bovand, S. Rashidi, J. Esfahani, Enhancement of heat transfer by nanofluids and orientations of the equilateral triangular obstacle, Energy Convers. Manage. 97 (2015) 212–223.
[18] K.M. Gangawane, Computational analysis of mixed convection heat transfer characteristics in lid-driven cavity containing triangular block with constant heat flux: effect of Prandtl and Grashof numbers, Int. J. Heat Mass Transf. 105 (2017) 34–57.
[19] D. Chatterjee, B. Mondal, Mixed convection heat transfer from an equilateral triangular cylinder in cross flow at low Reynolds numbers, Heat Transf. Eng. 36 (1) (2014) 123–133.
[20] T.-C. Jue, Numerical analysis of vortex shedding behind a porous square cylinder, Int. J. Numer. Methods Heat Fluid Flow 14 (5) (2004) 649–663.
[21] S. Bhattacharyya, S. Dhinakaran, A. Khalili, Fluid motion around and through a porous cylinder, Chem. Eng. Sci. 61 (13) (2006) 4451–4461.
[22] X. Chen, P. Yu, S. Winoto, H.-T. Low, Numerical analysis for the flow past a porous square cylinder based on the stress-jump interfacial-conditions, Int. J. Numer. Methods Heat Fluid Flow 18 (5) (2008) 635–655.
[23] P. Yu, Y. Zeng, T. Lee, H. Bai, H. Low, Wake structure for flow past and through a porous square cylinder, Int. J. Heat Fluid Flow 31 (2) (2010) 141–153.
[24] A. Hasan, B. Foss, S. Sagatun, Flow control of fluids through porous media, Appl. Math. Comput. 219 (7) (2012) 3323–3335.
[25] X. Chen, P. Yu, S. Winoto, H. Low, Numerical analysis for the flow past a porous trapezoidal-cylinder based on the stress-jump interfacial-conditions, Int. J. Numer. Methods Heat Fluid Flow 19 (2) (2009) 223–241.
[26] K. Nandakumar, J.H. Masliyah, Laminar flow past a permeable sphere, Can. J. Chem. Eng. 60 (2) (1982) 202–211.
[27] S. Rashidi, R. Masoodi, M. Bovand, M.S. Valipour, Numerical study of flow around and through a porous diamond cylinder in different apex angles, Int. J. Numer. Methods Heat Fluid Flow 24 (7) (2014) 1504–1518.
[28] M.S. Valipour, S. Rashidi, M. Bovand, R. Masoodi, Numerical modeling of flow around and through a porous cylinder with diamond cross section, Eur. J. Mech. B. Fluids 46 (2014) 74–81.
[29] P. Vainshtein, M. Shapiro, C. Gutfinger, Creeping flow past and within a permeable spheroid, Int. J. Multiph. Flow 28 (12) (2002) 1945–1963.
[30] N. Guerroudj, H. Kahalerras, Mixed convection in a channel provided with heated porous blocks of various shapes, Energy Convers. Manage. 51 (3) (2010) 505–517.

[31] N. Guerroudj, H. Kahalerras, Mixed convection in an inclined channel with heated porous blocks, Int. J. Numer. Methods Heat Fluid Flow 22 (7) (2012) 839–861.
[32] H.-W. Wu, R.-H. Wang, Mixed convective heat transfer past a heated square porous cylinder in a horizontal channel with varying channel height, J. Heat Transf. 133 (2) (2011) 022503.
[33] K. Vafai, Handbook of Porous Media, second ed., Crc Press, Taylor & Francis Group, Boca Raton, 2015.
[34] D.B. Ingham, I. Pop, Transport Phenomena in Porous Media, Elsevier, UK, 1998.
[35] I. Pop, D.B. Ingham, Transport Phenomena in Porous Media II, Elsevier, UK, 2002.
[36] A.A. Mohamad, Lattice Boltzmann Method: Fundamentals and Engineering Applications with Computer Codes, Springer Science & Business Media, London Dordrecht Heidelberg New York, 2011.
[37] Z. Guo, T. Zhao, Lattice Boltzmann model for incompressible flows through porous media, Phys. Rev. E 66 (3) (2002) 036304.
[38] Z. Guo, T. Zhao, A lattice Boltzmann model for convection heat transfer in porous media, Numer. Heat Transf. Part B 47 (2) (2005) 157–177.
[39] N. Martys, D.P. Bentz, E.J. Garboczi, Computer simulation study of the effective viscosity in Brinkman's equation, Phys. Fluids 6 (4) (1994) 1434–1439.
[40] M.A.A. Spaid, F.R. Phelan, Lattice Boltzmann methods for modeling microscale flow in fibrous porous media, Phys. Fluids 9 (9) (1997) 2468–2474.
[41] D.M. Freed, Lattice-Boltzmann method for macroscopic porous media modeling, Int. J. Mod. Phys. C 09 (08) (1998) 1491–1503.
[42] X. Nie, N.S. Martys, Breakdown of Chapman-Enskog expansion and the anisotropic effect for lattice-Boltzmann models of porous flow, Phys. Fluids 19 (1) (2007) 011702.
[43] I. Ginzburg, Consistent lattice Boltzmann schemes for the Brinkman model of porous flow and infinite Chapman-Enskog expansion, Phys. Rev. E 77 (6) (2008).
[44] H. Yoshida, H. Hayashi, Transmission–reflection coefficient in the lattice Boltzmann method, J. Stat. Phys. 155 (2) (2014) 277–299.
[45] G. Silva, I. Ginzburg, The permeability and quality of velocity field in a square array of solid and permeable cylindrical obstacles with the TRT–LBM and FEM Brinkman schemes, CR Méc 343 (10–11) (2015) 545–558.
[46] G. Silva, L. Talon, I. Ginzburg, Low- and high-order accurate boundary conditions: from Stokes to Darcy porous flow modeled with standard and improved Brinkman lattice Boltzmann schemes, J. Comput. Phys. 335 (2017) 50–83.
[47] S.D. Walsh, H. Burwinkle, M.O. Saar, A new partial-bounceback lattice-Boltzmann method for fluid flow through heterogeneous media, Comput. Geosci. 35 (6) (2009) 1186–1193.
[48] J. Zhu, J. Ma, An improved gray lattice Boltzmann model for simulating fluid flow in multi-scale porous media, Adv. Water Resour. 56 (2013) 61–76.
[49] M. Pepona, J. Favier, A coupled immersed boundary–lattice Boltzmann method for incompressible flows through moving porous media, J. Comput. Phys. 321 (2016) 1170–1184.
[50] I. Ginzburg, Comment on "An improved gray Lattice Boltzmann model for simulating fluid flow in multi-scale porous media": intrinsic links between LBE Brinkman schemes, Adv. Water Resour. 88 (2016) 241–249.
[51] Y. Hu, D. Li, S. Shu, X. Niu, Finite-volume method with lattice Boltzmann flux scheme for incompressible porous media flow at the representative-elementary-volume scale, Phys. Rev. E 93 (2) (2016).
[52] V. Babu, A. Narasimhan, Investigation of vortex shedding behind a porous square cylinder using lattice Boltzmann method, Phys. Fluids (1994-present) 22 (5) (2010) 053605.
[53] W. Minkowycz, A. Haji-Sheikh, K. Vafai, On departure from local thermal equilibrium in porous media due to a rapidly changing heat source: the Sparrow number, Int. J. Heat Mass Transf. 42 (18) (1999) 3373–3385.
[54] W.-S. Fu, H.-C. Huang, W.-Y. Liou, Thermal enhancement in laminar channel flow with a porous block, Int. J. Heat Mass Transf. 39 (10) (1996) 2165–2175.
[55] Q. Zou, X. He, On pressure and velocity boundary conditions for the lattice Boltzmann BGK model, Phys. Fluids (1994-present) 9 (6) (1997) 1591–1598.
[56] D.A. Nield, A. Bejan, Convection in Porous Media, Springer Science & Business Media, New York Heidelberg Dordrecht London, 2006.
[57] P.D. Noymer, L.R. Glicksman, A. Devendran, Drag on a permeable cylinder in steady flow at moderate Reynolds numbers, Chem. Eng. Sci. 53 (16) (1998) 2859–2869.
[58] A.J.C. Ladd, Numerical simulations of particulate suspensions via a discretized Boltzmann equation. Part 2. Numerical results, J. Fluid Mech. 271 (1994) 311.
[59] X. He, L.-S. Luo, Theory of the lattice Boltzmann method: from the Boltzmann equation to the lattice Boltzmann equation, Phys. Rev. E 56 (6) (1997) 6811.
[60] N. Sharma, A.K. Dhiman, S. Kumar, Mixed convection flow and heat transfer across a square cylinder under the influence of aiding buoyancy at low Reynolds numbers, Int. J. Heat Mass Transf. 55 (9) (2012) 2601–2614.
[61] D. Yu, R. Mei, L.-S. Luo, W. Shyy, Viscous flow computations with the method of lattice Boltzmann equation, Prog. Aerosp. Sci. 39 (5) (2003) 329–367.